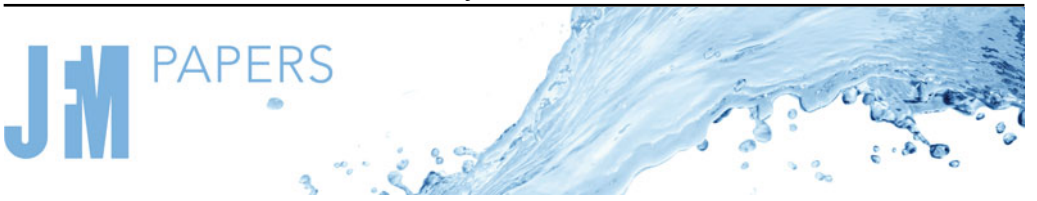
*J. Fluid Mech.* (2025), *vol.* 1015, A52, doi:10.1017/jfm.2025.10297




# Ill posedness in shallow multi-phase debris-flow models

**Jake Langham**[1], **Xiannan Meng**[2], **Jamie P. Webb**[1], **Chris G. Johnson**[1] **and J.M.N.T. Gray**[1]

[1]Department of Mathematics and Manchester Centre for Nonlinear Dynamics, University of Manchester, Oxford Road, Manchester M13 9PL, UK

[2]Transportation Engineering College, Dalian Maritime University, Dalian 116026, PR China

**Corresponding authors:** Jake Langham, jacob.langham@manchester.ac.uk; Xiannan Meng, xiannan.meng@dlmu.edu.cn

(Received 15 March 2025; revised 24 May 2025; accepted 26 May 2025)

Depth-averaged systems of equations describing the motion of fluid–sediment mixtures have been widely adopted by scientists in pursuit of models that can predict the paths of dangerous overland flows of debris. As models have become increasingly sophisticated, many have been developed from a multi-phase perspective in which separate, but mutually coupled sets of equations govern the evolution of different components of the mixture. However, this creates the opportunity for the existence of pathological instabilities stemming from resonant interactions between the phases. With reference to the most popular approaches, analyses of two- and three-phase models are performed, which demonstrate that they are more often than not ill posed as initial-value problems over physically relevant parameter regimes – an issue which renders them unsuitable for scientific applications. Additionally, a general framework for detecting ill posedness in models with any number of phases is developed. This is used to show that small diffusive terms in the equations for momentum transport, which are sometimes neglected, can reliably eliminate this issue. Conditions are derived for the regularisation of models in this way, but they are typically not met by multi-phase models that feature diffusive terms.

**Key words:** shallow water flows, wet granular material, mathematical foundations

## 1. Introduction

Debris flows are large-scale gravity currents that are formed on hillslopes when water entrains and mixes with rocks, mud and other natural detritus. Despite their daunting

© The Author(s), 2025. Published by Cambridge University Press. This is an Open Access article, distributed under the terms of the Creative Commons Attribution-ShareAlike licence (https://creativecommons.org/licenses/by-sa/4.0/), which permits re-use, distribution, and reproduction in any medium, provided the same Creative Commons licence is used to distribute the re-used or adapted article and the original article is properly cited.



https://doi.org/10.1017/jfm.2025.10297 Published online by Cambridge University Press

physical complexity, the threat they pose to human life (Dowling & Santi 2014) motivates ongoing efforts to develop detailed model descriptions of them, for the purposes of hazard prediction and risk assessment (Hutter, Svendsen & Rickenmann 1994; Iverson 1997; Trujillo-Vela *et al.* 2022).

The commonest class of available models are variations on the classical depth-averaged shallow-water equations, re-derived to incorporate physical effects particular to debris flows, such as non-Newtonian stresses, buoyancy and pore water pressure. Early approaches considered flows to be sufficiently homogeneous that the mass and momentum of fluid and submerged debris could be lumped together into a single continuous phase, subject to bulk conservation laws (Savage & Hutter 1989; Macedonio & Pareschi 1992; Iverson 1997; Fraccarollo & Papa 2000; Iverson & Denlinger 2001; Christen, Kowalski & Bartelt 2010). While this perspective is sometimes justified, it cannot fully account for important phenomena that arise from interactions between different components within the flow, such as changes in the debris composition due to dilation and particle size segregation, which can have a profound effect on the dynamics (Hutter *et al.* 1994; Iverson 1997; Berti *et al.* 2000; McCoy *et al.* 2010; Johnson *et al.* 2012). Consequently, some models have included an equation for the transport of an additional phase of solid particles within the flow, enabling solutions to develop compositional variations that may in turn affect the local fluid rheology (Takahashi *et al.* 1992; Shieh, Jan & Tsai 1996; Brufau *et al.* 2000). This approach may be augmented by introducing coupled equations for the evolution of the vertical distribution of solids (Kowalski & McElwaine 2013), or the basal pore-fluid pressure (George & Iverson 2014; Iverson & George 2014). A related strategy is to consider the transport of two or more species of granular material, while neglecting the presence of a carrier fluid (Gray & Kokelaar 2010). When combined with velocity shear through an assumed vertically segregated flow column and frictional dependence on particle size, this can likewise capture complex phenomena that are inaccessible to the simplest models, including thickened fronts that dam the flow (Denissen *et al.* 2019) and spontaneous finger formation (Woodhouse *et al.* 2012; Baker, Johnson & Gray 2016).

Truly 'multi-phase' systems take a step further by disaggregating the momentum dynamics of the different phases, thereby permitting the forces acting on each constituent to be modelled separately (Pitman & Le 2005; Pelanti, Bouchut & Mangeney 2008; Pailha & Pouliquen 2009; Pudasaini 2012; Bouchut *et al.* 2016; Li *et al.* 2018; Pudasaini & Mergili 2019; Meyrat *et al.* 2022; Meng *et al.* 2022, 2024). Model development in this final category is ongoing and promises to deliver the most faithful realisation of debris-flow physics within the depth-averaged framework, particularly when there is significant separation of phases within the flow.

However, the specification of separate momentum equations for multiple flow phases can introduce a fundamental pathology into depth-averaged models, causing them to no longer reflect the behaviour of the underlying physical system. For example, when a second fluid layer is added to the classical shallow-water equations, they cease to be unconditionally strictly hyperbolic (Ovsyannikov 1979), leaving the system ill posed as an initial-value problem when the flow is in certain conditions. The underlying reason for this is that buoyancy-mediated coupling between the two layers introduces a linear instability with a growth rate that diverges to infinity in the limit of high-wavenumber perturbations. A practical consequence of this is that time-dependent simulations of the system in these conditions are guaranteed to be mesh-dependent. Therefore, much attention has been given towards developing physically defensible methods which locally amend this model or otherwise drive solutions away from non-hyperbolic regimes (see e.g. Castro, Macías & Parés 2001; Sarno *et al.* 2017; Krvavica, Tuhtan & Jelenić 2018; Castro Díaz *et al.* 2023).



https://doi.org/10.1017/jfm.2025.10297 Published online by Cambridge University Press

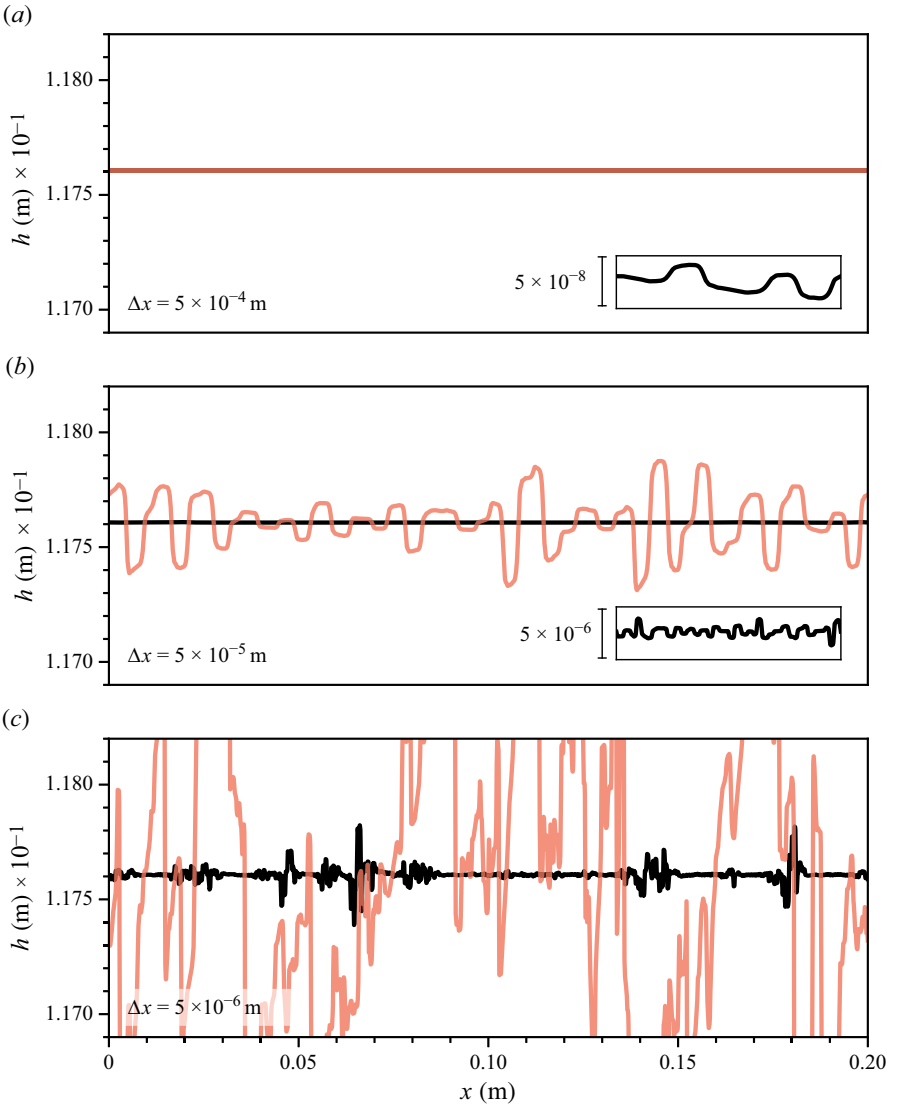



Figure 1. Demonstration of ill posedness, using the model of Meng *et al.* (2022). Snapshots of total flow depth ($h = H_f + H_s$ in the notation of § 2.2) at times $t = 1$ s (black) and 2 s (red) are plotted for numerical simulations of an initially uniform steady flow in a periodic domain of length 0.2 m, subject to a small noisy perturbation. (Full details of the simulation are given in Appendix A.) Successive panels show computations with increasingly refined numerical grids, with cell spacing $\Delta x =$ (*a*) $5 \times 10^{-4}$ m, (*b*) $5 \times 10^{-5}$ m and (*c*) $5 \times 10^{-6}$ m. The insets in (*a*,*b*) show the corresponding $t = 1$ s snapshots using shorter vertical axes, as indicated. Supplementary movie 1 available at https://doi.org/10.1017/jfm.2025.10297 shows an animation of the simulations.

Shallow debris-flow models with two phases possess a similar mathematical structure and can suffer from the same pathology. An illustration of this is depicted in figure 1, which shows successive attempts to numerically simulate a small perturbation to a steady uniform flow in the model of Meng, Johnson & Gray (2022), for conditions where strict hyperbolicity is lost. While at the coarsest resolution, there appears to be no instability, finer discretisations reveal oscillations. These develop more rapidly,



https://doi.org/10.1017/jfm.2025.10297 Published online by Cambridge University Press

and with higher spatial frequency as the grid is refined further. This is because each successive discretisation permits the approximation of higher-wavenumber modes, thereby inviting faster and faster growth. Any attempt to converge the simulation towards an underlying solution of the governing equations is guaranteed to fail, since there is no upper bound on growth rate, implying that the observed divergence of successive numerical solutions can never terminate. More precisely, no well-defined time-evolving solution of the continuous equations exists to converge upon. Full details of this computation are given in Appendix A.

Ill posedness presents a problem for any physical model and numerous examples have arisen in the fluid mechanics literature over the years (Joseph & Saut 1990). In particular, it has been discovered to affect mixed-sediment shallow-flow systems that feature particle segregation (Woodhouse *et al.* 2012; Baker *et al.* 2016) and bed morphodynamics (Cordier, Le & Morales de Luna 2011; Stecca, Siviglia & Blom 2014; Chavarrías *et al.* 2018, 2019; Langham *et al.* 2021). Furthermore, it was established long ago that the underlying mixture equations from which shallow multi-phase debris-flow models are derived can feature ill posedness in some cases (Bedford & Drumheller 1983; Drew 1983). Though these cases are obviously physically related, depth-averaged debris-flow systems are structurally inequivalent in general and require their own analyses that depend upon the particular assumptions employed to reach a shallow model description. There has been comparatively little work in this direction, possibly because the corresponding linear dispersion relations (which underlie the analysis of ill posedness) are at least quartic, making them very difficult to make sense of algebraically. The only substantial progress appears to be the analysis of Pelanti *et al.* (2008), who derived equations very similar to the model of Pitman & Le (2005) and provided inexact bounds on the flow properties that guarantee well posedness. Nevertheless, these bounds can be violated in situations accessible to realistic debris flows – a possibility which should trouble any operational modellers aiming to compute reliable simulations of these dangerous phenomena.

The following paper presents an investigation of this issue from a general framework that addresses many of the existing multi-phase models in the literature. Rather than attempting to identify conditions where models can be safely used, we instead take the view that any ill posedness within physically realistic limits is disqualifying for a model and look for situations where this can occur. Our analysis is sufficiently general in scope to establish the existence of ill posedness within the two-phase models of Pitman & Le (2005), Pelanti *et al.* (2008), Pudasaini (2012), Meyrat *et al.* (2022) and Meng *et al.* (2022), as well as in the three-phase model of Pudasaini & Mergili (2019). The two-phase models are introduced in § 2, as particular cases within a generalised shallow-layer description, and their posedness is analysed in § 3, along with a separate treatment of three-phase models. Furthermore, in § 4 we show that ill posedness may be alleviated in each of these models via the inclusion of neglected momentum diffusion terms. En route to this conclusion, a theoretical recipe is developed for assessing posedness that may be employed to analyse any model of $n$ phases and spatial derivatives of up to second order.

## 2. Depth-averaged theory

Consider a fluid medium consisting of $n$ continuous phases. Each phase $i$ consists of material of constant density $\rho_i$, flows with velocity $\boldsymbol{u}_i \equiv \boldsymbol{u}_i(\boldsymbol{x}, t)$ and occupies a fraction $\varphi_i \equiv \varphi_i(\boldsymbol{x}, t)$ of the mixture volume at each point in space $\boldsymbol{x}$ and time $t$. The interior of the flow is assumed to be saturated, so $\varphi_1 + \cdots + \varphi_n = 1$. In debris flows, the different phases may be either fluids, such as pure water or muddy suspensions, or distributions of small solid particles that are concentrated enough to transmit internal stresses. Although no single point may be simultaneously occupied by fluid and particles, the local volume



https://doi.org/10.1017/jfm.2025.10297 Published online by Cambridge University Press

fractions may be theoretically rationalised either via an explicit assumption that the phases are everywhere superposed, or by means of suitable averaging procedures defined over the microscale (Bedford & Drumheller 1983; Jackson 2000). While there are some technical differences between these approaches (Joseph *et al.* 1990), the resulting form of the governing equations for each phase in three spatial dimensions is well established (see e.g. Anderson & Jackson 1967; Drew 1983; Morland 1992). Assuming negligible surface tension at any interfaces and that no exchange of material occurs, either between phases or with the external environment, these may be written as

$$\frac{\partial \varphi_i}{\partial t} + \nabla \cdot (\varphi_i \boldsymbol{u}_i) = 0, \tag{2.1a}$$

$$\frac{\partial}{\partial t}(\rho_i \varphi_i \boldsymbol{u}_i) + \nabla \cdot (\rho_i \varphi_i \boldsymbol{u}_i \otimes \boldsymbol{u}_i) = \nabla \cdot \boldsymbol{\sigma}_i + \boldsymbol{f}_i - \rho_i \varphi_i \boldsymbol{g}, \tag{2.1b}$$

for $i = 1, \ldots, n$, where $\boldsymbol{\sigma}_i$ denotes an effective (or 'partial') stress tensor for each phase, $\boldsymbol{f}_i$ is the total force per unit volume acting on phase $i$ due to the others and $\boldsymbol{g}$ is acceleration due to gravity.

On the grounds that debris flows propagate over distances far greater than their characteristic thickness, the models that we study simplify (2.1*a*) and (2.1*b*) by averaging the motion over the flow depth. In addition to this assumption, two simplifications are made for ease of presentation that do not affect the generality of our primary conclusions. Firstly, we suppose that the flow propagates over a flat surface located at $z = 0$ through which there is no flux of material, and orient Cartesian spatial coordinates $\boldsymbol{x} = (x, y, z)$ so that $x$ and $y$ are parallel with this surface. Secondly, we enforce uniformity of flow in $y$ and hereafter drop consideration of this direction from the analysis. The flow is bounded above the base by a surface located at $z = h(x, t)$, which is assumed to be stress free. For any quantity $q(x, z, t)$, its depth-averaged counterpart $\overline{q}(x, t)$ is defined by

$$\overline{q}(x, t) = \frac{1}{h}\int_0^h q(x, z, t)\, \mathrm{d}z. \tag{2.2}$$

On averaging both sides of (2.1*a*) and (2.1*b*), one may obtain

$$\frac{\partial}{\partial t}(h\overline{\varphi_i}) + \frac{\partial}{\partial x}(h\overline{\varphi_i}\,\overline{u_i}) = 0, \tag{2.3a}$$

$$\frac{\partial}{\partial t}(\rho_i h\overline{\varphi_i}\,\overline{u_i}) + \frac{\partial}{\partial x}\left(\rho_i h\overline{\varphi_i}\,\overline{u_i}^2 - h\overline{\sigma_i^{xx}}\right) = h\overline{f_i^x} - \rho_i h\overline{\varphi_i} g^x - \sigma_i^{xz}|_{z=0}, \tag{2.3b}$$

where algebraic superscripts denote components of vectors and tensors in the corresponding Cartesian directions. The details involved in deriving the above equations follow standard methods and are not important here, except to note that wherever a product of depth-averaged quantities arises, we make use of the approximation

$$\overline{qr} = \overline{q}\,\overline{r}\left[1 + \frac{1}{h}\int_0^h \left(1 - \frac{q}{\overline{q}}\right)\left(1 - \frac{r}{\overline{r}}\right)\mathrm{d}z\right] \approx \overline{q}\,\overline{r}, \tag{2.4}$$

where $q$ and $r$ denote arbitrary fields. The relative error introduced by using this formula is quantified by the second term inside the square brackets of (2.4). It is small if the fields do not vary greatly over the flow depth. This is frequently assumed in operational models, including each of the systems that we focus on below.

The framework encapsulated by (2.3*a*) and (2.3*b*) is general enough to encompass most shallow multi-phase flow models. Different specialisations to the particular case of debris flows are made by specifying constitutive models for $\overline{\sigma_i^{xx}}$, $\overline{f_i^x}$ and the basal drag $\sigma_i^{xz}|_{z=0}$.



https://doi.org/10.1017/jfm.2025.10297 Published online by Cambridge University Press

These mostly involve a fluid phase of either pure water or water containing fine suspended sediments, and a solids phase of monodisperse grains. Therefore, for the remainder of this exposition, we simplify to two phases, labelled $f$ (fluids) and $s$ (solids). For convenience, a table is provided for this case in Appendix B, which cross-references our notation against the primary models covered below. Later, a three-phase model, due to Pudasaini & Mergili (2019), is analysed and its relevant features are specified separately in § 3.2 and Appendix C.

One ingredient that must be included within the interphase force terms is the buoyancy felt by the immersed particles. This is caused by the fluid pressure $p$ acting on the solid phase. Therefore, we write the force on the solids as

$$\boldsymbol{f}_s = -\varphi_s \nabla p + \boldsymbol{d}_s, \tag{2.5}$$

where $\boldsymbol{d}_s$ represents any other forces associated with the fluid phase acting on the solids and $p$ is the fluid pressure, which is implied to be hydrostatic at leading order, by the assumption of shallow flow (see e.g. Pitman & Le 2005; Meng *et al.* 2022). Hydrostatic pressure is determined by the weight of the fluid within in the water column:

$$p(z) = \rho_f g^z (h - z). \tag{2.6}$$

Therefore, on depth-averaging the slope-parallel component of (2.5), we obtain

$$h\overline{f_s^x} = -\rho_f g^z h \overline{\varphi_s} \frac{\partial h}{\partial x} + h\overline{d_s^x}. \tag{2.7}$$

By Newton's third law, an equal and opposite force $\overline{f_f^x} = -\overline{f_s^x}$ acts upon the fluid phase.

The remaining component of the interphase forces, $\boldsymbol{d}_s = -\boldsymbol{d}_f$, must include contributions due to their relative motion. In conditions close to equilibrium, this may be modelled with an appropriate closure depending on the relative velocity $\boldsymbol{u}_f - \boldsymbol{u}_s$ that captures the aggregate effect of drag between the two phases (Morland 1992; Jackson 2000). However, if one phase accelerates into the other, this induces an additional transfer of momentum between the phases, which can also be included (Anderson & Jackson 1967). The force on individual particles associated with this is called the 'added' or 'virtual' mass effect and depends on the relative accelerations in a frame following the particle (Maxey & Riley 1983). It is unclear how best to aggregate this into a force acting on a collective phase of particles, so approaches differ (Anderson & Jackson 1967; Bedford & Drumheller 1983; Drew 1983). One option, favoured by Pudasaini (2012) in the derivation of their debris-flow model, defines the added mass force on the solids to be

$$\boldsymbol{M}_s = C\rho_f \varphi_s \left( \frac{\partial \boldsymbol{u}_f}{\partial t} + \boldsymbol{u}_f \cdot \nabla \boldsymbol{u}_f - \frac{\partial \boldsymbol{u}_s}{\partial t} - \boldsymbol{u}_s \cdot \nabla \boldsymbol{u}_s \right), \tag{2.8}$$

where $C$ is a positive coefficient (that may depend on the flow variables, in particular, the volume fraction). Depth-averaging this term proceeds in the same way as for the convective terms on the left-hand side of the governing equations and leads to

$$h\overline{M_s^x} = \overline{C'} \left[ \frac{\partial}{\partial t}(\rho_f h \overline{\varphi_f}\, \overline{u_f}) + \frac{\partial}{\partial x}(\rho_f h \overline{\varphi_f}\, \overline{u_f}^2) \right] - \gamma \overline{C} \left[ \frac{\partial}{\partial t}(\rho_s h \overline{\varphi_s}\, \overline{u_s}) + \frac{\partial}{\partial x}(\rho_s h \overline{\varphi_s}\, \overline{u_s}^2) \right], \tag{2.9}$$

where $\gamma \equiv \rho_f/\rho_s$ and $C' \equiv C\varphi_s/\varphi_f$. An opposing force $\overline{M_f^x} = -\overline{M_s^x}$ must likewise appear in the depth-averaged momentum equation for the fluid phase.

The remaining terms to be specified are: the depth-averaged lateral stresses $\overline{\sigma_i^{xx}}$, the basal stresses $\sigma_i^{xz}|_{z=0}$ and any remaining depth-averaged forces $h(\overline{d_i^x} - \overline{M_i^x})$ (such as



https://doi.org/10.1017/jfm.2025.10297 Published online by Cambridge University Press

drag between the phases, for example). The choice of the lateral stress components is responsible for most of the key differences that affect the analysis of models in this paper. Therefore, these are given with reference to particular models in the subsections below. The other two terms will not be given explicitly. Only terms containing time or space derivatives of the flow fields affect the analysis in the rest of this paper, and typically, neither $\sigma_i^{xz}|_{z=0}$ nor $\overline{d_i^x}$ carry dependence on gradient information. Therefore, these are left arbitrary and notation is subsequently simplified by defining

$$S_i = (\rho_i h\overline{\varphi_i})^{-1}\left[h\left(\overline{d_i^x} - \overline{M_i^x}\right) - \rho_i h\overline{\varphi_i} g^x - \sigma_i^{xz}|_{z=0}\right] \tag{2.10}$$

for use in the following subsections. The factor of $1/(\rho_i h\overline{\varphi_i})$ is included to account for the fact that the momentum equations will shortly be multiplied through by this quantity in the course of converting them to quasilinear form.

### 2.1. *Pitman and Le's model*

The assumption of shallow flow, used in deriving (2.3*a*) and (2.3*b*), may also be used to infer from the slope-normal component of (2.1*b*) that at leading order the normal stresses are in equilibrium with the interphase forces and gravity:

$$\frac{\partial \sigma_i^{zz}}{\partial z} = -f_i^z + \rho_i \varphi_i g^z. \tag{2.11}$$

In deriving their debris-flow model, Pitman & Le (2005) use this to obtain expressions for the stresses. The fluid tensor is assumed to be isotropic and the slope-normal interphase forces are considered to be dominated by buoyancy, so $d_s^z = 0$ and from (2.5), $f_s^z = -\varphi_s \partial p/\partial z = -f_f^z$. Substituting this into (2.11), depth-integrating twice and using (2.6), gives

$$\sigma_f^{zz} = -\rho_f g^z (h - z) \quad \text{and} \quad \overline{\sigma_f^{xx}} = \overline{\sigma_f^{zz}} = -\frac{1}{2}\rho_f g^z h. \tag{2.12a,b}$$

Note that the direction of the buoyancy force and gravity coincide to make the effective stress for the fluid phase equal to the intrinsic pressure $p$ of the fluid. Conversely, for the solids phase, buoyancy acts against gravity to reduce the effective normal stress to

$$\sigma_s^{zz} = -\varphi_s(\rho_s - \rho_f) g^z (h - z). \tag{2.13}$$

Since the flow is anticipated to be densely packed with grains, principles of soil mechanics are invoked to infer a proportional relationship between lateral and normal stresses, via an Earth pressure coefficient $K$:

$$\sigma_s^{xx} = K\sigma_s^{zz}. \tag{2.14}$$

On depth-averaging and using (2.14), one may therefore deduce that

$$-\frac{\partial}{\partial x}\left(h\overline{\sigma_s^{xx}}\right) = \frac{\partial}{\partial x}\left[\frac{1}{2}K(1-\gamma)\rho_s g^z \overline{\varphi_s} h^2\right]. \tag{2.15}$$

The model may be expressed in full by substituting (2.7), (2.12*b*) and (2.15) into (2.3*a*) and (2.3*b*) and algebraically simplifying. It is convenient at this stage to define variables that express the proportion of the mixture depth occupied by each phase:

$$H_i = \overline{\varphi_i} h. \tag{2.16}$$

Using these variables and noting in particular that $h = H_s + H_f$, the following set of equations are obtained:



https://doi.org/10.1017/jfm.2025.10297 Published online by Cambridge University Press

$$\frac{\partial H_s}{\partial t} + \frac{\partial}{\partial x}(H_s \overline{u_s}) = 0, \tag{2.17a}$$

$$\frac{\partial \overline{u_s}}{\partial t} + \overline{u_s}\frac{\partial \overline{u_s}}{\partial x} + g^z\left[\gamma + K(1-\gamma)\left(1 + \frac{H_f}{2H_s}\right)\right]\frac{\partial H_s}{\partial x} + g^z\left[\gamma + \frac{K}{2}(1-\gamma)\right]\frac{\partial H_f}{\partial x} = S_s, \tag{2.17b}$$

$$\frac{\partial H_f}{\partial t} + \frac{\partial}{\partial x}(H_f \overline{u_f}) = 0, \tag{2.17c}$$

$$\frac{\partial \overline{u_f}}{\partial t} + \overline{u_f}\frac{\partial \overline{u_f}}{\partial x} + g^z\frac{\partial H_s}{\partial x} + g^z\frac{\partial H_f}{\partial x} = S_f. \tag{2.17d}$$

The particular case of $K = 1$ was studied in detail by Pelanti *et al.* (2008).

### 2.2. *Meng et al.'s model*

The model of Meng *et al.* (2022) is derived using a conceptually different description of the flow that posits separate free surfaces for the depth of solid particles $h_s$ and depth of fluid $h_f$. When $h_f > h_s$, the particles are 'oversaturated' with fluid and assumed to have settled into a layer at the bottom of the flow, within which they occupy a constant volume fraction $\varphi_c$. We consider this case only, since the analysis of Meng *et al.* (2024) (in their Appendix A) establishes that their model equations in the 'undersaturated' regime $h_f < h_s$ are hyperbolic, with a differential operator whose structure decouples into separate shallow-layer terms for each phase, thereby leading to well-posed initial-value problems.

The solids stresses take the same form as in the Pitman & Le (2005) model's (2.13), except they are only present up to the height $h_s$ of the solids layer, implying that the term inside the pressure derivative of (2.15) differs by a factor of $h_s/h_f$. Moreover, $K = 1$ is assumed. Therefore,

$$-\frac{\partial}{\partial x}\left(h\overline{\sigma_s^{xx}}\right) = \frac{\partial}{\partial x}\left[\frac{1}{2}(1-\gamma)\rho_s g^z \overline{\varphi_s} h_s h_f\right]. \tag{2.18}$$

Additionally, the viscous component of the fluid stress tensor is retained. Therefore, rather than appealing to (2.11), the constitutive relation

$$\boldsymbol{\sigma}_f = -p\boldsymbol{I} + \varphi_f \eta_f\left[\nabla \boldsymbol{u}_f + (\nabla \boldsymbol{u}_f)^T\right] \tag{2.19}$$

is proposed, where $\eta_f$ is the dynamic viscosity of the fluid. The intrinsic pore fluid pressure is hydrostatic as before, so (2.6) applies and consequently,

$$-\frac{\partial}{\partial x}\left(h\overline{\sigma_f^{xx}}\right) = \rho_f g^z h_f \frac{\partial h_f}{\partial x} - \frac{\partial}{\partial x}\left(2\eta_f h_f \overline{\varphi_f}\frac{\partial \overline{u_f}}{\partial x}\right). \tag{2.20}$$

To obtain the final term on the right, $\overline{\partial u_f/\partial x} \approx \partial \overline{u_f}/\partial x$ is used, which follows from an assumption of low shear in the velocity profile $\overline{u_f} \approx u_f(h)$, and is consistent with the approximation made in (2.4).

Averaging the solids volume fraction over the full depth gives $\overline{\varphi_s} = \varphi_c h_s/h_f$. This implies that the equivalent partial depths (2.16) in this model are

$$H_s = \varphi_c h_s, \quad H_f = h_f - \varphi_c h_s. \tag{2.21}$$

On making these transformations, the derivative terms in the Meng *et al.* (2022) model equations are the same as the Pitman & Le (2005) model's (2.17*a–d*), save for the components related to the different formulations for internal stresses. Therefore, we report only the solid and fluid momentum equations, which may be obtained by substituting (2.18)



https://doi.org/10.1017/jfm.2025.10297 Published online by Cambridge University Press

and (2.20), along with the buoyancy forces (2.7), into (2.3*b*), using (2.21) and simplifying, leading to

$$\frac{\partial \overline{u_s}}{\partial t} + \overline{u_s}\frac{\partial \overline{u_s}}{\partial x} + g^z\left[\gamma + \frac{1-\gamma}{\varphi_c}\right]\frac{\partial H_s}{\partial x} + g^z\gamma\frac{\partial H_f}{\partial x} = S_s, \tag{2.22a}$$

$$\frac{\partial \overline{u_f}}{\partial t} + \overline{u_f}\frac{\partial \overline{u_f}}{\partial x} + g^z\frac{\partial H_s}{\partial x} + g^z\frac{\partial H_f}{\partial x} = \frac{2\eta_f}{\rho_f H_f}\frac{\partial}{\partial x}\left(H_f\frac{\partial \overline{u_f}}{\partial x}\right) + S_f. \tag{2.22b}$$

A typical choice for the solids fraction constant in the regimes relevant to this model might be expected to lie somewhere in the range $0.5 \lesssim \varphi_c \lesssim 0.75$ (Pierson 1995). Nevertheless, it should be noted that in the limit $\varphi_c \to 1$ (where there are no saturated gaps between particles) and assuming also that $\eta_f = 0$, (2.22*a*) and (2.22*b*) together with (2.17*a*) and (2.17*c*) reduce to a system of depth-averaged equations for the motion of two immiscible fluids of different densities, whose properties have been widely studied (see e.g. Ovsyannikov 1979; Vreugdenhil 1979; Castro *et al.* 2001; Abgrall & Karni 2009; Kurganov & Petrova 2009; Chiapolino & Saurel 2018). A model of this latter type has also been proposed by Meyrat *et al.* (2022), for use in debris-flow modelling.

### 2.3. *Pudasaini's model*

Pudasaini (2012) uses an approach that is consistent with Pitman & Le (2005), but extends their framework in various ways. Of relevance to our analysis are the inclusion of the added mass term given previously in (2.9) and a fluid stress tensor that incorporates a non-Newtonian component.

The inclusion of added mass augments the inertial terms in the momentum equations. The coefficient $\overline{C}$ in (2.9) is assumed to be a constant. Furthermore, in order to simplify the conservative form of the equations Pudasaini (2012) makes the assumption that $\overline{C'} \equiv \overline{C}\,\overline{\varphi_s}/\overline{\varphi_f}$ may be absorbed into the time and space derivatives of (2.9) without explicitly holding it constant. This does not appear to be justified in our view. Nevertheless, summing the added mass force terms for each phase with the corresponding inertial terms from (2.3*b*) and converting to quasilinear form (i.e. by dividing through by $\rho_i H_i$ and simplifying) leads to

$$(1+\gamma\overline{C})\left(\frac{\partial \overline{u_s}}{\partial t} + \overline{u_s}\frac{\partial \overline{u_s}}{\partial x}\right) - \gamma\overline{C}\left(\frac{\partial \overline{u_f}}{\partial t} + \overline{u_f}\frac{\partial \overline{u_f}}{\partial x}\right) - \underbrace{\frac{\gamma\overline{C}\,\overline{u_f}}{H_s}\left[\frac{\partial H_s}{\partial t} + \frac{\partial}{\partial x}\left(H_s\overline{u_f}\right)\right]}_{\text{extra terms}}, \tag{2.23a}$$

$$\left(1+\frac{\overline{C}H_s}{H_f}\right)\left(\frac{\partial \overline{u_f}}{\partial t} + \overline{u_f}\frac{\partial \overline{u_f}}{\partial x}\right) - \frac{\overline{C}H_s}{H_f}\left(\frac{\partial \overline{u_s}}{\partial t} + \overline{u_s}\frac{\partial \overline{u_s}}{\partial x}\right) + \overbrace{\frac{\overline{C}\,\overline{u_f}}{H_f}\left[\frac{\partial H_s}{\partial t} + \frac{\partial}{\partial x}\left(H_s\overline{u_f}\right)\right]}, \tag{2.23b}$$

for the inertia of the solids and fluid phases, respectively. The extra terms, highlighted by the braces, do not appear if (2.9) is depth-averaged directly and could arguably be omitted, since they correspond to a force between the phases whose physical origin is unclear. However, in order to analyse the model as it has appeared in prior publications, we retain them.

The assumed form of the fluid stress tensor is equal to the expression used by Meng *et al.* (2022), given in (2.19), plus an additional phenomenological component

$$-\eta_f\mathcal{A}\left[\nabla\varphi_s \otimes (\boldsymbol{u}_f - \boldsymbol{u}_s) + (\boldsymbol{u}_f - \boldsymbol{u}_s)\otimes\nabla\varphi_s\right], \tag{2.24}$$



https://doi.org/10.1017/jfm.2025.10297 Published online by Cambridge University Press

where $\mathcal{A}$ is a parameter that depends on the solids fraction. After adding on the Newtonian component, depth-averaging $\sigma_f^{xx}$ gives

$$-\frac{\partial}{\partial x}\left(h\overline{\sigma_f^{xx}}\right)=\rho_f g^z h\frac{\partial h}{\partial x}-\frac{\partial}{\partial x}\left(2\eta_f h\overline{\varphi_f}\frac{\partial\overline{u_f}}{\partial x}-2\eta_f\overline{\mathcal{A}}h(\overline{u_f}-\overline{u_s})\frac{\partial\overline{\varphi_s}}{\partial x}\right) \tag{2.25}$$

for this model, where we have used $\overline{\partial\varphi_s/\partial x}\approx\partial\overline{\varphi_s}/\partial x$, which is consistent with the assumption of negligible variation in volume fraction over the depth, $\overline{\varphi_s}\approx\varphi_s(h)$. In the original derivation, Pudasaini (2012) goes further, following an approach of Iverson & Denlinger (2001) for averaging diffusive stresses by bringing $h$ outside the spatial derivatives of (2.25). This introduces extra terms, which, under the stress-free boundary condition, reduce to expressions that do not contain derivatives and may be modelled separately as source terms (Pudasaini 2012). These extra steps do not affect the forthcoming analysis of the model structure (since the linearised diffusion operator remains the same). Therefore, we leave (2.25) as it is.

## 3. Local analysis

We will demonstrate that the two-phase models outlined in the previous section, as well as straightforward three-phase extensions to these systems, contain flow regimes where the equations are ill posed as initial-value problems. This is because under certain conditions, infinitesimal disturbances blow up with linear growth rates that increase without bound in the limit of high spatial frequencies, leaving the equations without solutions – a pathological property sometimes known as a 'Hadamard instability' (Joseph & Saut 1990).

### 3.1. *Two-phase models*

Given some putative model solution with fields $\boldsymbol{q}=(H_s,\overline{u_s},H_f,\overline{u_f})^T$, we would like to understand the local behaviour of the governing equations at an arbitrary space–time location $(x_0,t_0)$. Denote a state vector there by

$$\boldsymbol{q}_0=\boldsymbol{q}(x_0,t_0)=\left(H_s^{(0)},\ \overline{u_s}^{(0)},\ H_f^{(0)},\ \overline{u_f}^{(0)}\right)^T. \tag{3.1}$$

We assume non-vanishing fluid depth $H_f^{(0)}>0$ and velocity $\overline{u_f}^{(0)}\neq 0$, so that the governing equations for each model may be non-dimensionalised with respect to these scales. States may then be fully characterised by three dimensionless quantities:

$$R_H=H_s^{(0)}/H_f^{(0)},\quad R_u=\overline{u_s}^{(0)}/\overline{u_f}^{(0)},\quad Fr=\frac{\overline{u_f}^{(0)}}{\sqrt{g^z H_f^{(0)}}}, \tag{3.2a–c}$$

where $Fr$ is the local Froude number for the fluid phase. Therefore, hereafter the transformations

$$x\mapsto x/H_f^{(0)},\quad t\mapsto t\overline{u_f}^{(0)}/H_f^{(0)},\quad H_i\mapsto H_i/H_f^{(0)},\quad \overline{u_i}\mapsto\overline{u_i}/\overline{u_f}^{(0)},$$
$$S_i\mapsto S_i H_f^{(0)}/(\overline{u_f}^{(0)})^2 \tag{3.3a–e}$$

are made to the two-phase models analysed. Furthermore, note that the systems detailed in §§ 2.1–2.3 may be collectively cast in the general form

$$\boldsymbol{A}(\boldsymbol{q})\frac{\partial\boldsymbol{q}}{\partial t}+\boldsymbol{B}(\boldsymbol{q})\frac{\partial\boldsymbol{q}}{\partial x}=\boldsymbol{S}(\boldsymbol{q})+\boldsymbol{D}_1(\boldsymbol{q})\frac{\partial}{\partial x}\left(\boldsymbol{D}_2(\boldsymbol{q})\frac{\partial\boldsymbol{q}}{\partial x}\right), \tag{3.4}$$



https://doi.org/10.1017/jfm.2025.10297 Published online by Cambridge University Press

where $\boldsymbol{S}(\boldsymbol{q}) = (0,\, S_s,\, 0,\, S_f)^T$ and $\boldsymbol{A}$, $\boldsymbol{B}$, $\boldsymbol{D}_1$, $\boldsymbol{D}_2$ are matrices of (dimensionless) variable coefficients that that may be readily specified for each model.

We now 'freeze' the solution, by assuming that $\boldsymbol{q}(x,t) = \boldsymbol{q}_0$ within a local neighbourhood of $(x_0, t_0)$ and consider the evolution of a normal-mode perturbation $\boldsymbol{r}\exp(\mathrm{i}kx + \sigma t)$ to this state, where $k$ is a real-valued wavenumber, $\sigma$ a complex growth rate and $\boldsymbol{r}$ a vector constant with $|\boldsymbol{r}| \ll |\boldsymbol{q}_0|$. Linearising (3.4) around the frozen base state $\boldsymbol{q}_0$ leads to the following eigenproblem for the pair $(\sigma, \boldsymbol{r})$:

$$\sigma \boldsymbol{A}(\boldsymbol{q}_0)\boldsymbol{r} + \mathrm{i}k\boldsymbol{B}(\boldsymbol{q}_0)\boldsymbol{r} = \boldsymbol{C}(\boldsymbol{q}_0)\boldsymbol{r} - k^2\boldsymbol{D}(\boldsymbol{q}_0)\boldsymbol{r}, \tag{3.5}$$

where $\boldsymbol{C} \equiv \partial \boldsymbol{S}/\partial \boldsymbol{q}$ and $\boldsymbol{D} = \boldsymbol{D}_1\boldsymbol{D}_2$. If $\boldsymbol{q}_0$ happens to represent a state for which the model equations admit steady uniform flow, i.e. $\boldsymbol{S}(\boldsymbol{q}_0) = \boldsymbol{0}$, then the solutions to (3.5) dictate the linear stability of such a flow, for which $\mathrm{Re}(\sigma) > 0$ indicates an unstable mode and the case of Hadamard instability occurs if $\mathrm{Re}(\sigma) \to \infty$ as $k \to \infty$, indicating that the governing equations (3.4) are ill posed at $\boldsymbol{q}_0$. Otherwise, the procedure of freezing the base state is justified insofar as it may be used to identify this latter pathology on the grounds that any candidate solution $\boldsymbol{q}$ must be effectively constant near $(x_0, t_0)$, when measured with respect to the infinitesimal length and time scales over which the Hadamard instability develops (Joseph & Saut 1990; Joseph 1990).

Since diffusion can be small, relative to other terms in the equations, it is sometimes desirable to neglect its effects. Therefore, we first consider the case where $\boldsymbol{D}$ is the zero matrix. It may then straightforwardly be determined from (3.5) that in the asymptotic limit of high $k$, the leading-order components of the growth rates for the four eigenmodes are $\sigma = -\mathrm{i}k\lambda_j$, where $\lambda_j$ $(j = 1, \ldots, 4)$ denote the characteristic wave speeds of the problem, given by the solutions to the generalised eigenproblem $\boldsymbol{B}\boldsymbol{r} = \lambda_j\boldsymbol{A}\boldsymbol{r}$. If all four are real and distinct then the system is said to be 'strictly hyperbolic' at $\boldsymbol{q}_0$ and is well posed as an initial-value problem. On the other hand, any complex characteristics must arise in conjugate pairs. Since one of the pair must have $\mathrm{Im}(\lambda_j) > 0$, the corresponding real part of $\sigma$ is positive and scales as $O(k)$ for $k \gg 1$, giving rise to a Hadamard instability. Repeated real characteristics can also lead to growth rate blow-up, but the reasons for this are more subtle. This case is covered later in § 4.1.

### 3.1.1. *Emergence of ill posedness*

The inclusion of added mass leads to complications, which we address shortly, in §§ 3.1.2 and 4.3.2. If it is neglected, then $\boldsymbol{A}$ simplifies to the identity matrix $\boldsymbol{I}$ and the problem reduces to computing the eigenvalues of the Jacobian $\boldsymbol{B}$, which has the same essential form for each of the models. Bearing in mind our transformation to dimensionless variables in (3.3*a*–*e*), this matrix is

$$\boldsymbol{B}(\boldsymbol{q}) = \begin{pmatrix} \overline{u_s} & H_s & 0 & 0 \\ (\gamma+\beta_1)Fr^{-2} & \overline{u_s} & (\gamma+\beta_2)Fr^{-2} & 0 \\ 0 & 0 & \overline{u_f} & H_f \\ Fr^{-2} & 0 & Fr^{-2} & \overline{u_f} \end{pmatrix}, \tag{3.6}$$

where $\beta_1 = K(1-\gamma)[1 + H_f/(2H_s)]$, $\beta_2 = K(1-\gamma)/2$ for Pitman & Le (2005) and Pudasaini (2012); $\beta_1 = (1-\gamma)/\varphi_c$, $\beta_2 = 0$ in Meng *et al.* (2022); and $\beta_1 = 1-\gamma$, $\beta_2 = 0$ for two-fluid models (e.g. Ovsyannikov 1979), as well as the debris-flow model of Meyrat *et al.* (2022). Note that at $\boldsymbol{q} = \boldsymbol{q}_0$, $H_s = R_H$, $\overline{u_s} = R_u$ and $H_f = \overline{u_f} = 1$.

The possibility for $\boldsymbol{B}(\boldsymbol{q}_0)$ to have complex characteristics arises due to the coupling between the momentum equations provided by the entries $B_{23}$ and $B_{41}$. Physically, these



https://doi.org/10.1017/jfm.2025.10297 Published online by Cambridge University Press

terms arise because the buoyancy and solids stresses depend on the total depth $H_s + H_f$. For systems without this coupling, i.e. $B_{23} = B_{41} = 0$, the eigenvalues of $\boldsymbol{B}(\boldsymbol{q}_0)$ are

$$\lambda_s^{\pm} \equiv R_u \pm \frac{\sqrt{R_H(\gamma + \beta_1)}}{Fr} \quad \text{and} \quad \lambda_f^{\pm} \equiv 1 \pm \frac{1}{Fr}. \tag{3.7a,b}$$

These are real provided $\beta_1 + \gamma > 0$. For the model closures described above, this is certainly the case, since both $\beta_1$ and $\gamma$ are strictly positive. While the corresponding expressions for the eigenvalues of $\boldsymbol{B}(\boldsymbol{q}_0)$ in the general case, $B_{23}, B_{41} \neq 0$, can be computed via the quartic formula, these are are too complicated to be especially useful (Pitman & Le 2005; Pelanti *et al.* 2008; Pudasaini 2012). Nevertheless, since $\boldsymbol{B}(\boldsymbol{q}_0)$ is almost block diagonal, its characteristic polynomial is amenable to further analysis.

In particular, one can generalise an approach followed by Ovsyannikov (1979) for the simpler two-fluid case ($\beta_1 = 1 - \gamma$, $\beta_2 = 0$) and notice that the eigenvalues $\lambda_j$ are determined by an equation of the form

$$f(P_1, P_2) \equiv (P_1^2 - 1)(P_2^2 - 1) = c, \tag{3.8}$$

where

$$P_1^2 = \frac{(\lambda_j - R_u)^2 Fr^2}{R_H(\gamma + \beta_1)}, \quad P_2^2 = (\lambda_j - 1)^2 Fr^2 \quad \text{and} \quad c = \frac{\gamma + \beta_2}{\gamma + \beta_1}. \tag{3.9a–c}$$

For a particular point in parameter space, characterised by the triple $(R_H, R_u, Fr)$, we can eliminate $\lambda_j$ from (3.9*a*,*b*) to determine that the characteristics lie on the intersection of the line

$$P_2 = P_1\sqrt{R_H(\gamma + \beta_1)} + Fr(R_u - 1) \tag{3.10}$$

with the level set given by the contour of the surface $f(P_1, P_2)$ (3.8) at the value $c$. This is depicted graphically in figure 2(*a*). Coloured contours in the figure show the surface $f(P_1, P_2)$, with an example level at $c = 1/3$ given by the solid black curves. Three dash–dot black lines illustrate possibilities for the characteristics. The line labelled I represents a strictly hyperbolic case, since it possesses four distinct intersections with the solid black contour. On shifting the line upwards to II (by increasing $Fr(R_u - 1)$) the characteristics associated with the central contour merge to form a complex conjugate pair and only two real solutions to (3.8) and (3.10) remain. Shifting the line further up recovers strict hyperbolicity, since at position III, it makes two additional intersections with the portion of the level set that is confined to $\{(P_1, P_2) : P_1 < -1, P_2 > 1\}$. Provided that $c > 0$ and that $\beta_1$, $\beta_2$ are either constants or a functions of $R_H$ only, as is the case for the models considered herein, we can see that there will always be an ill-posed region associated with the loss of strict hyperbolicity (i.e. regions without four distinct real eigenvalues). This is because a given $R_H$ fixes the level set determined by $c$. Then, varying $Fr(R_u - 1)$ shifts the dash–dotted lines in the $P_2$ direction, guaranteeing that they pass through a region with only two intersections. Indeed, by symmetry, there must be two such regions.

This framework encapsulates the analysis by Pitman & Le (2005) who showed for their model that cases close to $R_u = 1$ are always strictly hyperbolic. This is a consequence of the fact that the (3.10) lines pass through the origin at this point. Moreover, Pelanti *et al.* (2008) later gave bounds on $|R_u - 1|$ that guarantee well posedness for sufficiently small and sufficiently large values.

The white dashed lines in figure 2 show the level set contours at $c = 0$, given by $P_1 = \pm 1$, $P_2 = \pm 1$. In this special case, the characteristics are everywhere real and it is straightforward to see that they must be the same as the values for uncoupled systems, given in (3.7*a*,*b*). Moreover, each point $(\pm 1, \pm 1)$ may be linked to one of the four possible



https://doi.org/10.1017/jfm.2025.10297 Published online by Cambridge University Press

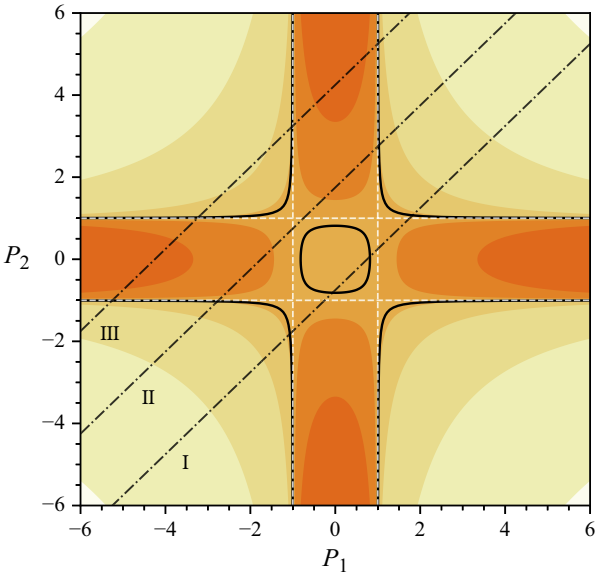



Figure 2. Geometric analysis of the characteristics for two-phase models. Filled contours of the surface $f(P_1, P_2)$ are plotted, spaced at intervals $\pm 10^m$ for $m = 0, \ldots, 4$. The zero contour is marked separately (white dashed), as is the level set at $c = 1/3$ (black solid). Dash–dotted lines are $P_2 = P_1 - 0.75 + 2n$, for $n = 0, 1, 2$.

intersections between the solid ($\lambda_s^{\pm}$) and fluid ($\lambda_f^{\pm}$) characteristics. For example, let $R_u$, $R_H$ be fixed and suppose that $R_u > 1$, implying that the dash–dotted lines of figure 2 (3.10) intercept the $P_2$ axis at positive values. From examination of the expressions for the characteristics in (3.7*a*,*b*), it may determined that there always exists a $Fr$ such that $\lambda_s^- = \lambda_f^+$ in this case. Moreover, depending on whether the gradients of the dash–dot lines $\sqrt{R_H(\gamma + \beta_1)}$ are greater or less than unity, the respective intersections $\lambda_s^- = \lambda_f^-$ and $\lambda_s^+ = \lambda_f^+$ are possible. By considering (geometrically) the corresponding options for the lines to pass through $(\pm 1, \pm 1)$ in this case, we infer that $\lambda_s^- = \lambda_f^+$ corresponds to the point $(-1, 1)$ and likewise that $\lambda_s^- = \lambda_f^-$ corresponds to $(-1, -1)$ and $\lambda_s^+ = \lambda_f^+$ to $(1, 1)$. Symmetric reasoning for the case $R_u < 1$ determines the final intersection, $\lambda_s^+ = \lambda_f^-$ at $(1, -1)$. The important points are $(-1, 1)$ and $(1, -1)$, when the positive and negative branches coincide. This occurs when

$$R_u = 1 \pm \frac{1}{Fr}\left[1 + \sqrt{R_H(\gamma + \beta_1)}\right]. \tag{3.11}$$

It is from these intersections that the complex eigenvalues of $\boldsymbol{B}(\boldsymbol{q}_0)$ emerge when the system is fully coupled. Therefore, the consequent blow-up in growth rate in these regions can be thought of as stemming from a resonant interaction between the characteristic wave speeds of the solid and fluid phases.

In figures 3(*a*) and 3(*b*), we plot the regions where ill posedness occurs for the Pitman & Le (2005) and Meng *et al.* (2022) models, respectively (without diffusion), in terms of $R_H$ and $|Fr(R_u - 1)|$. Note that these two parameters fully determine whether the characteristics are real-valued or not. As already inferred from the geometric analysis, the models are unconditionally well posed when $R_u = 1$ and at sufficiently high values of $|Fr(R_u - 1)|$. Furthermore, the bands of ill posedness are organised around the condition



https://doi.org/10.1017/jfm.2025.10297 Published online by Cambridge University Press

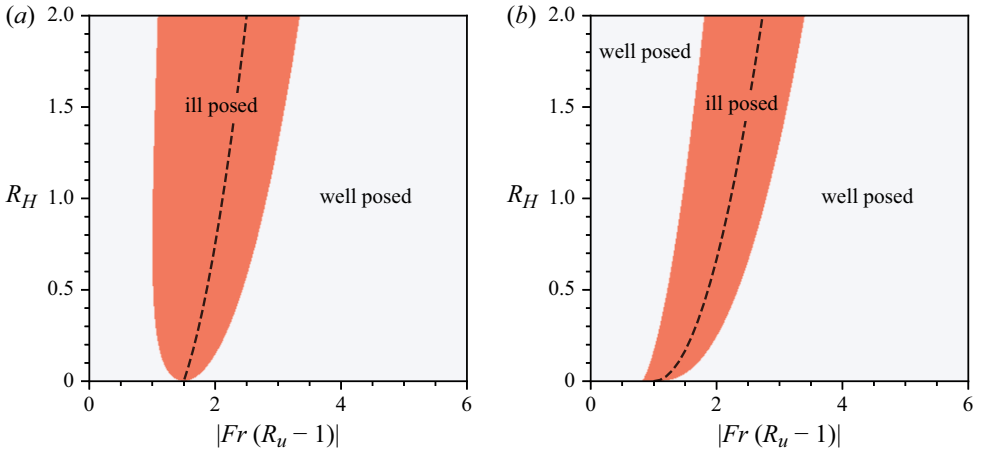



Figure 3. Regions of parameter space which contain complex characteristics, indicated by the red shaded regions, for the models of (*a*) Pitman & Le (2005) with $\gamma = 0.5$, $K = 1$ and (*b*) Meng *et al.* (2022) with $\gamma = 0.5$, $\varphi_c = 0.5$. In the case of (*b*), the parameter choices correspond to the solid black level set in figure 2. Outside the shaded regions, the characteristics are real and distinct. The black dashed curves are where positive and negative branches of characteristics from the corresponding uncoupled problems intersect, as given in (3.11).

in (3.11) (black dashed lines). The width of the bands is contingent on the model parameters, which select the level set(s) in figure 2, and the qualitative differences in shape between the bands for the two models are explained by the different dependence. Specifically, while the level set value $c$ for the Meng *et al.* (2022) model is fixed, for Pitman & Le (2005), $c \equiv c(R_H)$ with $c \to 0$ as $R_H \to 0$. This implies that the width of the figure 3(*a*) band approaches zero in this limit. Conversely, when $c$ is constant, the band has a finite width as $R_H \to 0$, determined by the minimum distance between the central piece of the figure 2 level set and any of the lines $P_1$, $P_2 = \pm 1$, which are asymptotically approached by the other sections of the level set. A brief calculation shows that this is $1 - \sqrt{1 - c}$ for $c \in [0, 1]$, or 1 for $c > 1$ (where in this latter case there is no central piece of the level set). Additionally, the uncoupled characteristic intersections must lie at the upper limit of the band as $R_H \to 0$. Combining these observations with (3.11) determines that the interval $(\sqrt{1 - c}, 1)$ remains ill posed in this case, as $R_H \to 0$. This property is demonstrated for the Meng *et al.* (2022) model with $c = 1/3$, by examining figure 3(*b*).

### 3.1.2. *Added mass effect*

When the added mass effect is included in the two-phase model of Pudasaini (2012), many additional terms are introduced that cause the equations to be more strongly coupled. Though this model also contains diffusive terms, it is informative to investigate first how the incorporation of this additional physics affects the model's eigenstructure in the absence of diffusion. One reason for this is that, at least in some cases, ill posedness in some non-depth-averaged two-phase flow systems without diffusion can be regularised by including added mass terms (Drew 1983).

On introducing added mass effects by generalising the inertial terms in the solids and fluid momentum equations to the expressions given previously in (2.23*a*) and (2.23*b*),



https://doi.org/10.1017/jfm.2025.10297 Published online by Cambridge University Press

respectively, the matrices $\boldsymbol{A}$ and $\boldsymbol{B}$ become

$$\boldsymbol{A} = \begin{pmatrix} 1 & 0 & 0 & 0 \\ -\gamma\overline{C}\,\overline{u_f}H_s^{-1} & 1+\gamma\overline{C} & 0 & -\gamma\overline{C} \\ 0 & 0 & 1 & 0 \\ \overline{C}\,\overline{u_f}H_f^{-1} & -\overline{C}H_sH_f^{-1} & 0 & 1+\overline{C}H_sH_f^{-1} \end{pmatrix}, \tag{3.12}$$

$$\boldsymbol{B} = \begin{pmatrix} \overline{u_s} & H_s & 0 & 0 \\ (\gamma+\beta_1)Fr^{-2} - \frac{\gamma\overline{C}\,\overline{u_f}^2}{H_s} & (1+\gamma\overline{C})\overline{u_s} & (\gamma+\beta_2)Fr^{-2} & -2\gamma\overline{C}\,\overline{u_f} \\ 0 & 0 & \overline{u_f} & H_f \\ Fr^{-2} + \overline{C}\,\overline{u_f}^2H_f^{-1} & -\overline{C}\,\overline{u_s}H_sH_f^{-1} & Fr^{-2} & \overline{u_f} + \frac{2\overline{C}\,\overline{u_f}H_s}{H_f} \end{pmatrix}. \tag{3.13}$$

When the added mass coefficient $\overline{C}$ is non-zero, the corresponding characteristic polynomial $p_c(\lambda) = \det(\boldsymbol{B} - \lambda\boldsymbol{A})$ for this system lacks the advantageous structure that was leveraged in the previous section to analyse the eigenvalues geometrically. Nevertheless, they are straightforward to obtain numerically at any point in parameter space. On doing so, it was found (as might well be expected) that the boundaries of the well-posed regions do not collapse neatly onto curves in terms of the parameters $R_H$ and $Fr(R_u - 1)$, as before. However, it is possible to observe the qualitative effect of increasing $\overline{C}$ from zero.

The plots in figure 4 show an illustrative example, in which $\gamma = 0.5$, $R_H = 1$ and $\overline{C}$ is incremented up to the value of 0.5 suggested by Pudasaini (2012). When $\overline{C} = 0$, the system reduces to the structure of the Pitman & Le (2005) model. The ill-posed regions lie either side of $R_u = 1$ and take the form of bands around the curves given previously in (3.11). Increasing $\overline{C}$ to 0.1 results in a slight narrowing of the 'upper' band with $R_u > 1$ and a slight thickening of the lower $R_u < 1$ band. Additionally, a new region of complex characteristics emerges beneath the lower band at higher Froude numbers. This region extends further towards lower $Fr$ when $\overline{C}$ is increased to 0.5 (figure 4*c*), leaving most of the $R_u < 1$ half-plane ill posed. Furthermore, the upper band separates into two pieces, leaving a well-posed region in between them. Moreover, a small region of ill posedness appears at an $R_u$ closer to unity. It is approximately centred around the point $(Fr,\ R_u) = (3.04,\ 1.05)$. We inspected equivalent plots for other choices of $\gamma$ and $R_H$ in the ranges $0.3 < \gamma < 0.8$, $0.2 < R_H < 1.5$ and found them to be qualitatively similar.

These results indicate that the added mass force in this case does little to ameliorate the problem of ill posedness on its own and arguably seems to make matters worse, especially when the fluids velocity greatly exceeds the solids velocity ($R_u < 1$) – a situation which could be encountered when a less concentrated debris flow entrains a static pile of grains, for example. Some analytical insight into the emergence of the large ill-posed region for $R_u < 1$ is gained later in § 4.3.2.

### 3.2. *Three-phase models*

For three-phase models that share the same essential structure as the two-phase models we have analysed, it is possible to generalise the geometric reasoning of § 3.1.1 to identify regions of parameter space that must contain complex characteristics, provided the added mass effect is negligible.



https://doi.org/10.1017/jfm.2025.10297 Published online by Cambridge University Press

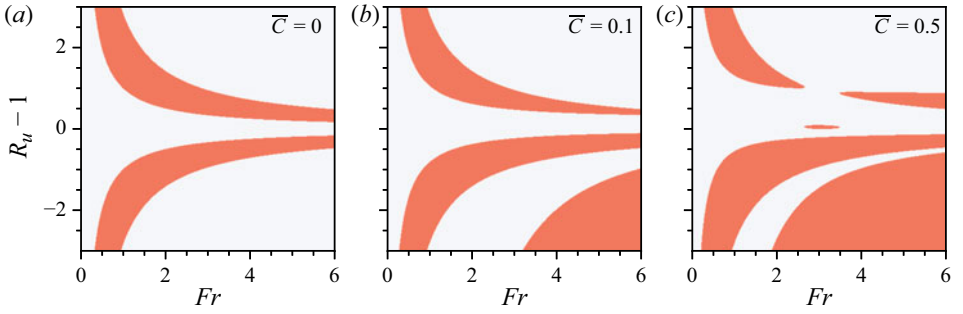



Figure 4. Effect of added mass terms in the Pudasaini (2012) model without diffusion. Regions of parameter space that possess complex characteristics are shaded red, for $R_H = 1$, $\gamma = 0.5$ and $\overline{C} =$ (*a*) 0, (*b*) 0.1 and (*c*) 0.5.

Therefore, we return to the case $\overline{C} = 0$, $\boldsymbol{A} = \boldsymbol{I}$ and consider models that possess a Jacobian of the form

$$\boldsymbol{B} = \begin{pmatrix} \overline{u_1} & H_1 & 0 & 0 & 0 & 0 \\ \beta_{11} & \overline{u_1} & \beta_{12} & 0 & \beta_{13} & 0 \\ 0 & 0 & \overline{u_2} & H_2 & 0 & 0 \\ \beta_{21} & 0 & \beta_{22} & \overline{u_2} & \beta_{23} & 0 \\ 0 & 0 & 0 & 0 & \overline{u_3} & H_3 \\ \beta_{31} & 0 & \beta_{32} & 0 & \beta_{33} & \overline{u_3} \end{pmatrix}, \tag{3.14}$$

where $H_i$ denote partial heights for each phase, $\overline{u_i}$ the corresponding downstream velocities and $\beta_{ij}$ represent arbitrary functions of these flow variables. This generalises the essential structure of the two-phase Jacobian in (3.6) to three phases. Denote the characteristic polynomial of this matrix by $p_c$. By direct computation, it may be shown that $p_c(\lambda) = 0$ simplifies to

$$f(P_1, P_2, P_3) \equiv \prod_{i=1}^{3}(P_i^2 - 1) - (P_1^2 - 1)\frac{\beta_{23}\beta_{32}}{\beta_{22}\beta_{33}} - (P_2^2 - 1)\frac{\beta_{13}\beta_{31}}{\beta_{11}\beta_{33}} - (P_3^2 - 1)\frac{\beta_{12}\beta_{21}}{\beta_{11}\beta_{22}} = c, \tag{3.15}$$

where

$$P_i^2 = \frac{(\overline{u_i} - \lambda)^2}{\beta_{ii} H_i} \quad \text{and} \quad c = \frac{\beta_{13}\beta_{21}\beta_{32} + \beta_{12}\beta_{23}\beta_{31}}{\beta_{11}\beta_{22}\beta_{33}} > 0, \tag{3.16}$$

for $i = 1, 2, 3$. We retain the convention adopted previously, by non-dimensionalising with respect to the depth and velocity of the third phase, represented by the final two governing equations and hereafter assumed to represent the carrier fluid. There are now two pairs of relevant dimensionless quantities associated with the relative heights and velocities of the phases:

$$R_{H_1} = H_1^{(0)}/H_3^{(0)}, \quad R_{H_2} = H_2^{(0)}/H_3^{(0)}, \quad R_{u_1} = \overline{u_1}^{(0)}/\overline{u_3}^{(0)}, \quad R_{u_2} = \overline{u_2}^{(0)}/\overline{u_3}^{(0)}, \tag{3.17a–d}$$

alongside the Froude number for the fluid phase $Fr = \overline{u_3}^{(0)}/\sqrt{g^z H_3^{(0)}}$. On making the appropriate non-dimensionalising transformations and eliminating $\lambda$ from among the



https://doi.org/10.1017/jfm.2025.10297 Published online by Cambridge University Press

defining relations for the $P_i$ coordinates in (3.16), it may be concluded that the number of real roots of $p_c$ at a given point in parameter space is determined by the intersections of the level surface defined in (3.15) and (3.16), with the line given by the map

$$P_3 \mapsto \left( \frac{R_{u_1} - 1}{\sqrt{\beta_{11} R_{H_1}}} + P_3 \sqrt{\frac{\beta_{33}}{\beta_{11} R_{H_1}}}, \frac{R_{u_2} - 1}{\sqrt{\beta_{22} R_{H_2}}} + P_3 \sqrt{\frac{\beta_{33}}{\beta_{22} R_{H_2}}}, P_3 \right). \tag{3.18}$$

To illustrate the resulting geometric picture, we use the model of Pudasaini & Mergili (2019), which extends the two-phase system of Pudasaini (2012) to incorporate an intermediate fraction of fine solid particles. When added mass effects are neglected, the Jacobian for this model matches the structure given in (3.14). If the equations are organised such that the first two rows denote the solid phase, the second two the fine-solid phase and the final two the fluid phase, then the (non-dimensionalised) $\beta_{ij}$ closure terms are

$$\beta_{11} = \frac{1}{Fr^2} \left[ 1 + \frac{1}{2}(1 - \gamma_1) \left( \frac{R_{H_1} + R_{H_2} + 1}{R_{H_1}} \right) \right], \tag{3.19a}$$

$$\beta_{12} = \beta_{13} = \frac{1}{2Fr^2}(1 + \gamma_1) \tag{3.19b}$$

and $\beta_{2i} = \gamma_2 / Fr^2$, $\beta_{3i} = 1/Fr^2$, for $i = 1, 2, 3$, where $\gamma_1$ is the ratio of fluid to solid densities and $\gamma_2$ is the ratio of fluid to fine-solid densities. These latter two parameters are fixed material constants. On substituting the expressions for $\beta_{ij}$ into (3.15), (3.16) and (3.18), it may be deduced that both the level surface $f(P_1, P_2, P_3) = c$ and the gradient of the line in (3.18) depend only on the flow via the relative heights $R_{H_1}$ and $R_{H_2}$. Consequently, for a given $(R_{H_1}, R_{H_2})$ pair, the number of intersections between the line and the level set is determined by the remaining degrees of freedom for the line, namely the terms

$$K_1 \equiv \frac{R_{u_1} - 1}{\sqrt{\beta_{11} R_{H_1}}} \quad \text{and} \quad K_2 \equiv \frac{R_{u_2} - 1}{\sqrt{\beta_{22} R_{H_2}}}. \tag{3.20a,b}$$

By substituting in the appropriate values for $\beta_{11}$, $\beta_{22}$, it may be seen that $K_i \propto Fr(R_{u_i} - 1)$.

In figure 5, we plot the surface corresponding to the case $R_{H_1} = R_{H_2} = 1$ and $\gamma_1 = \gamma_2 = 0.5$. It consists of nine disjoint pieces, comprising eight surfaces in each corner octant, which we label 1–8 for later reference, and a central 'cross-shaped' surface. Far from the origin, the corner surfaces asymptote to the planes $P_i = \pm 1$. This is a consequence of the more general property that in the limit $|P_i| \to \infty$, (3.15) reduces to the two-dimensional level set corresponding to the equivalent two-phase problem with phase $i$ removed. This also explains the extended stems of the central cross, since slices of the surface in the far-field limits $|P_2| \to \infty$ and $|P_3| \to \infty$ (removing either of the fluid phases) may be compared with the two-phase level set in figure 2(*a*), with the stems of the cross giving rise to the closed curve around the origin.

Also plotted in figure 5 is the corresponding line with $K_1 = K_2 = 0$, which passes through (0, 0, 0). Using the fact that $\beta_{21} = \beta_{22} = \beta_{23}$ and $\beta_{31} = \beta_{32} = \beta_{33}$ for this model, it may be verified that the origin is an additional isolated point on the level set. Since the line also necessarily passes through the central cross surface and the corner surfaces 1 and 8, it intersects with the level set five times in total. Therefore, this case corresponds to a repeated real root of $p_c$. More generically, we should expect an even number of purely real eigenvalues, determined by the number of intersections of the plotted line through the origin after undertaking an appropriate translation in the $(P_1, P_2)$ plane by $(K_1, K_2)$,



https://doi.org/10.1017/jfm.2025.10297 Published online by Cambridge University Press

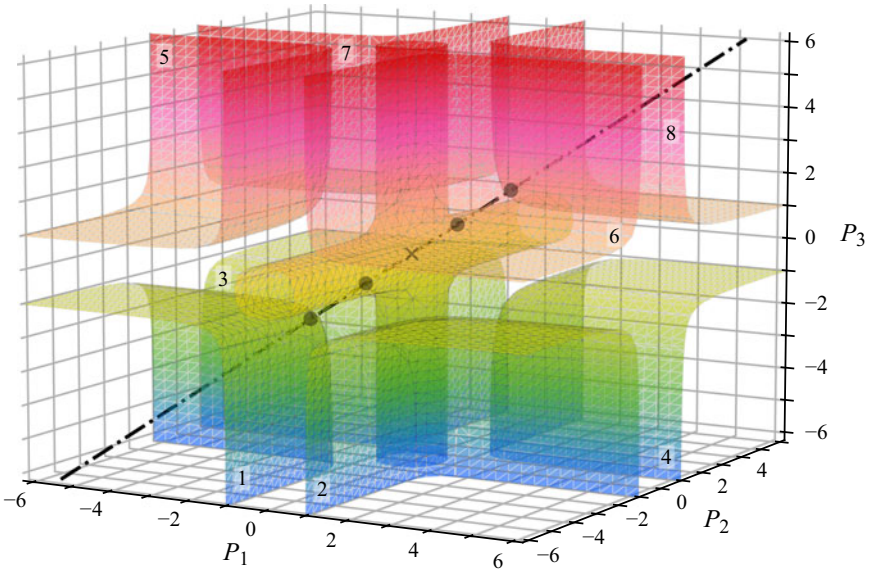



Figure 5. The surface $f(P_1, P_2, P_3) = c$, for the three-phase model of Pudasaini & Mergili (2019), with $\gamma_1 = \gamma_2 = 0.5$ and $R_{H_1} = R_{H_2} = 1$. For visual clarity, the disjoint pieces of the surface are rendered with a triangular mesh and coloured from blue to red according to the value of the $P_3$ coordinate. Also plotted is the line defined by (3.18) for $R_{u_1} = R_{u_2} = 1$. This intersects with the surface at the four points marked with circles and at the origin (marked with a cross), which is an additional isolated solution of $f(P_1, P_2, P_3) = c$, in this case. Supplementary movie 2 shows an animated view of the surface.

depending on the values of $Fr(R_{u_i} - 1)$ at a given point in parameter space. The different possibilities are summarised in figure 6. In particular, figure 6($a$) plots, as a function of $(K_1, K_2)$, whether there are six real roots (white), four real roots (pink) or only two (red). Cases where there are repeated real roots are associated with either tangential intersections between the line and level set (the borders of each shaded region in figure 6$a$) or isolated points such as the origin. Regions with complex eigenvalues cover a substantial part of the plane. Notably, the model is ill posed as an initial-value problem in this case for all $(K_1, K_2) \in [-1, 1]^2$, i.e. when

$$|R_{u_1} - 1| \leqslant \sqrt{\beta_{11} R_{H_1}} \quad \text{and} \quad |R_{u_2} - 1| \leqslant \sqrt{\beta_{22} R_{H_2}}. \tag{3.21a}$$

From the geometric picture in figure 5, we see that this is because there are only four available intersections in these cases (excepting the special case $R_{u_1} = R_{u_2} = 1$, already discussed). This observation contrasts with the two-phase models analysed above, which are always well posed when $R_u$ is sufficiently close to unity.

There are various other possibilities when $R_{u_1}$ or $R_{u_2}$ are large enough to lie outside the intervals in (3.21$a$). The diagrams in figure 6($b$–$d$) are useful for visualising them. These plots show how the intersections of the line and level set change as the line is translated along different trajectories in the $(K_1, K_2)$ plane, represented by dashed lines in figure 6($a$). The first of these, in figure 6($b$), considers translations with $K_2 = -K_1$. When $|K_1| < 1.06$ (3 s.f.), four intersections are identified, as already discussed. However, when $1.06 < |K_1| < 2.30$ (3 s.f.), two intersections are lost, since the line no longer passes through the central cross-shaped surface. On increasing $|K_1|$ further, two pairs of intersections are created with corner surfaces (2 and 6 for $K_1 > 2.30$, 3 and 7 for $K_1 < -2.30$), ultimately leading to well-posed regions when $|K_1| > 3.43$ (3 s.f.).



https://doi.org/10.1017/jfm.2025.10297 Published online by Cambridge University Press

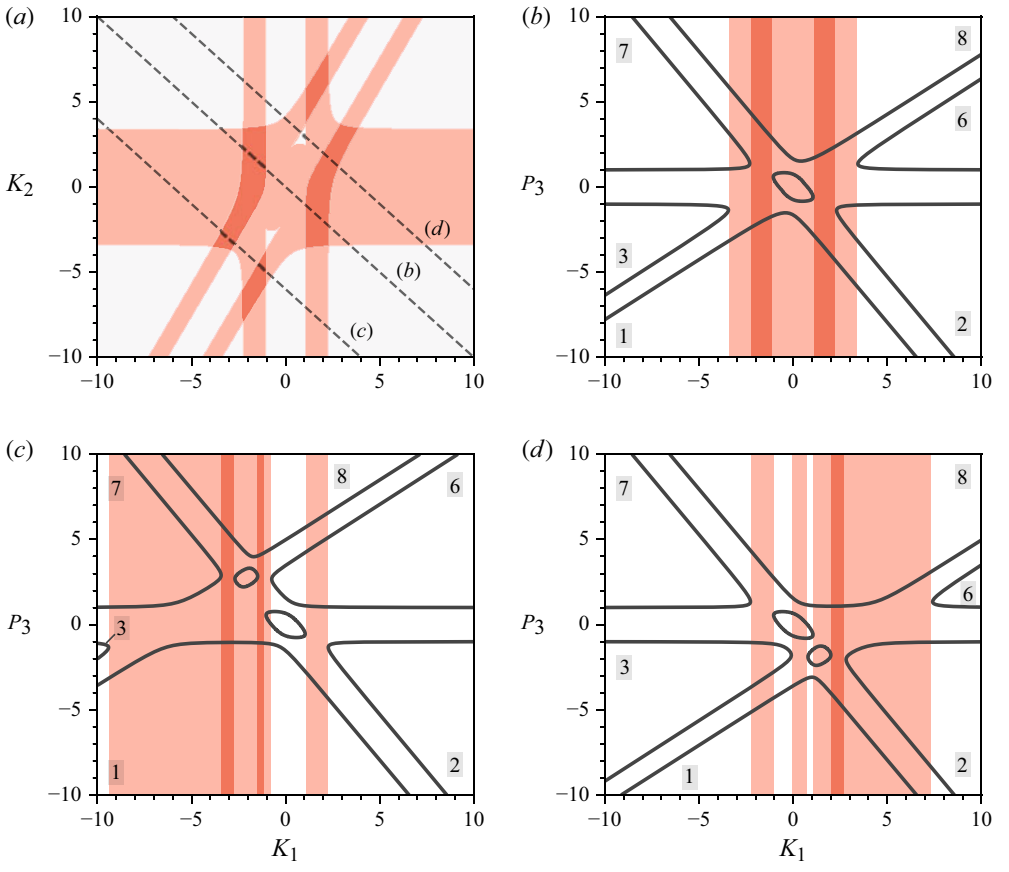



Figure 6. (*a*) Regions of the $(K_1, K_2)$ plane, for which the $(R_{H_1} = R_{H_2} = 1)$ surface geometry in figure 5 gives rise to six (white), four (pink) or two (red) real eigenvalues. (*b–d*) Intersections between the (3.18) line and the (3.15) level surface (solid lines), for $(K_1, K_2)$ values along the corresponding dashed lines plotted in (*a*). These are: (*b*) $K_2 = -K_1$, (*c*) $K_2 = -K_1 - 6$ and (*d*) $K_2 = -K_1 + 4$. The shaded bands indicate the number of intersections, in accordance with the colouring in (*a*). Labels denote regions enclosed by the numbered corner surfaces (see figure 5).

Figure 6(*c*) shows translations with $K_2 = -K_1 - 6$. In this case, when $K_1 = 0$, the line passes out of region 1, through the arm of the cross that extends along the $P_1 = 0$ plane and clips the sixth corner surface before passing into region 8, leading to six intersections. Larger $K_1$ values lead to a band of complex characteristics ($1.04 < K_1 < 2.26$, 3 s.f.), where the line misses the cross arm. When $K_1$ is lowered from zero, it misses region 6 and the cross arm in turn, leaving only two intersections for $-1.48 < K_1 < -1.04$ (3 s.f.). In the interval $-2.69 < K_1 < -1.48$ (3 s.f.), the line again intersects with the cross surface, this time through the arm extending along the $P_3$ axis. Lowering $K_1$ further leads to intersections with the seventh and third corner surfaces for $K_1 < -3.42$ (3 s.f.) and $K_1 < -9.40$ (3 s.f.) respectively. Finally, the intersections depicted in figure 6(*d*), which cover translations along $K_2 = -K_1 + 4$, are similar, but highlight an additional case: for $0.786 < K_1 < 1.05$ (3 s.f), the line clips through both arms of the cross, leading to a small well-posed band. Translations farther from the origin can also lead to intersections with regions 4 and 5.



https://doi.org/10.1017/jfm.2025.10297 Published online by Cambridge University Press

Varying $R_{H_1}$ and $R_{H_2}$ alters both the line and the level set. However, our earlier observation that the limits $|P_i| \to \infty$ reduce to two-phase models implies that the resulting parameter space must always contain ill-posed regions. This is likewise true for any model of the form given by (3.14). Therefore, while there may exist other three-phase models that possess more favourable properties near the origin (a fully general analysis would require us to classify all surfaces of the form given in (3.15)), none of these systems can be unconditionally well posed. Returning to the example case of the Pudasaini & Mergili (2019) model, an investigation of different values in the ranges $R_{H_1}, R_{H_2} \in [0.1, 10]$ led to regions of complex characteristics that qualitatively match the plot in figure 6(*a*), suggesting that the observations made thus far are robust across parameter space. It should be noted that in its full generality, this model also includes the option to include added mass forces and diffusive stresses. Though the presence of former terms alters the system's characteristic structure, the § 3.1.2 analysis of the corresponding two-phase case does little to suggest that they will substantially improve matters. The effect of diffusion is dealt with in the next section.

## 4. Regularisation

The question of how best to alleviate the ill posedness in these models is fraught with difficulty. Its presence in model equations is usually attributed to neglected physical effects (Joseph & Saut 1990). For example, in the related case of two-layer fluid models, the emergence of complex characteristics has been linked to the impossibility of resolving the vertical mixing induced by Kelvin–Helmholtz instabilities within a depth-averaged set of governing equations (Castro *et al.* 2001). However, the physics of debris flows are far from settled and the relative importance of neglected effects may depend on the specifics of a particular flow. Moreover, it is highly challenging to measure debris flows *in situ*, which removes the possibility of examining interior flow instabilities.

Nevertheless, an obvious candidate to investigate is longitudinal diffusion of momentum, since it is already included in some models and provides a clear mechanism for damping instabilities at high wavenumber. For example, in the typical case where $\boldsymbol{A} = \boldsymbol{I}$, it is straightforward to show that a full rank diffusion matrix $\boldsymbol{D}$ in (3.5) prohibits $\mathrm{Re}(\sigma)$ from blowing up as $k \to \infty$, provided all its eigenvalues are positive. However, since there is no clear reason to include diffusion in the equations for mass conservation, $\boldsymbol{D}$ generally will not be full rank and a deeper analysis is required.

### 4.1. *A general framework for finding Hadamard instabilities*

We return to the linear stability problem given in (3.5). A general procedure for detecting the presence or absence of Hadamard instabilities is developed. Since it is cast as an arbitrary matrix equation, there is no restriction on the dimensionality $N$ of the system, so our analysis in this subsection is applicable to models with any number of phases $n = N/2$. Readers that would rather skip the linear algebra may proceed to the final paragraph of this subsection, where the method for determining posedness is recapitulated.

First, we bring (3.5) into a simpler form for analysis. The matrix $\boldsymbol{A}$ must be invertible, in order for there to be $N$ independent time-evolving fields. Furthermore, we assume that the matrix $\boldsymbol{A}^{-1}\boldsymbol{D}$ is diagonalisable, since this covers all the specific cases in this paper. Then, the problem may be reformulated in terms of a basis $\{\hat{\boldsymbol{e}}_1, \ldots, \hat{\boldsymbol{e}}_N\}$ with respect to which $\boldsymbol{A}^{-1}\boldsymbol{D}$ is diagonal. Therefore, for each matrix $\boldsymbol{M} \in \{\boldsymbol{B}, \boldsymbol{C}, \boldsymbol{D}\}$, we define

$$\hat{\boldsymbol{M}} = \boldsymbol{P}^{-1}\boldsymbol{A}^{-1}\boldsymbol{M}\boldsymbol{P} \quad \text{and} \quad \hat{\boldsymbol{v}} = \boldsymbol{P}^{-1}\boldsymbol{v}, \tag{4.1a,b}$$



https://doi.org/10.1017/jfm.2025.10297 Published online by Cambridge University Press

for any vector $\boldsymbol{v}$, where $\boldsymbol{P}$ is a basis change matrix that diagonalises $\boldsymbol{A}^{-1}\boldsymbol{D}$. With respect to this transformation, (3.5) becomes

$$\sigma\hat{\boldsymbol{r}} + \mathrm{i}k\hat{\boldsymbol{B}}\hat{\boldsymbol{r}} = \hat{\boldsymbol{C}}\hat{\boldsymbol{r}} - k^2\hat{\boldsymbol{D}}\hat{\boldsymbol{r}}. \tag{4.2}$$

At high wavenumber $k \gg 1$, we make the following asymptotic expansions:

$$\sigma = -\sigma_2 k^2 - \mathrm{i}\sigma_1 k + \sigma_0 + \ldots, \quad \hat{\boldsymbol{r}} = \hat{\boldsymbol{r}}_0 + k^{-1}\hat{\boldsymbol{r}}_{-1} + \ldots, \tag{4.3a,b}$$

substitute them into (4.2) and look for the leading-order terms. Therefore, at $O(k^2)$, the problem reduces to

$$\hat{\boldsymbol{D}}\hat{\boldsymbol{r}}_0 = \sigma_2\hat{\boldsymbol{r}}_0. \tag{4.4}$$

Noting the sign convention in (4.3a,b), the eigenvalues $\sigma_2$, which represent diffusion coefficients for the linear problem, must each have non-negative real part in order to avoid blow-up of $\mathrm{Re}(\sigma)$. The growth of modes with $\sigma_2 = 0$ is determined beyond this leading-order balance. If $\hat{\boldsymbol{D}}$ is not full rank, it has $i \in \{1, \ldots, N\}$ zero eigenvalues. Without loss of generality, we locate these in the first $i$ diagonal values of $\hat{\boldsymbol{D}}$. The corresponding eigenvectors are determined only up to an $i$-dimensional subspace ($\hat{\boldsymbol{r}}_0 \in \mathrm{span}\{\hat{\boldsymbol{e}}_1, \ldots, \hat{\boldsymbol{e}}_i\}$) by (4.4).

Therefore, we proceed to the $O(k)$ part of the asymptotic expansion of (4.2). When $\sigma_2 = 0$, this is

$$(\hat{\boldsymbol{B}} - \sigma_1\boldsymbol{I})\hat{\boldsymbol{r}}_0 = \mathrm{i}\hat{\boldsymbol{D}}\hat{\boldsymbol{r}}_{-1}. \tag{4.5}$$

Since $\hat{\boldsymbol{r}}_0 \in \mathrm{span}\{\hat{\boldsymbol{e}}_1, \ldots, \hat{\boldsymbol{e}}_i\}$, only the first $i$ columns of $\hat{\boldsymbol{B}} - \sigma_1\boldsymbol{I}$ enter into this system of equations on the left-hand side. Furthermore, only the first $i$ rows of (4.5) are needed to determine $\hat{\boldsymbol{r}}_0$ and these are rows for which the right-hand side is zero. Consequently, the $\sigma_1$ values are the eigenvalues of the matrix $\hat{\boldsymbol{B}}$ with the last $N - i$ rows and columns removed. We write $\boldsymbol{M}_{red}$ to denote any matrix $\boldsymbol{M}$ reduced in this way by deleting rows and columns associated with the nullspace of the diagonal matrix $\hat{\boldsymbol{D}}$. Referring back to (4.3a,b), we obtain a second criterion that must be met to avoid Hadamard instability: the eigenvalues $\sigma_1$ of $\hat{\boldsymbol{B}}_{red}$ must be real. If these values are also distinct, then the growth rates stay bounded as $k \to \infty$.

However, $\hat{\boldsymbol{B}}_{red}$ may have repeated eigenvalues, which can also lead to blow-up of $\mathrm{Re}(\sigma)$. To see why, we proceed to the $O(1)$ equation with $\sigma_2 = 0$, which reads

$$(\sigma_0\boldsymbol{I} - \hat{\boldsymbol{C}})\hat{\boldsymbol{r}}_0 + \mathrm{i}(\hat{\boldsymbol{B}} - \sigma_1\boldsymbol{I})\hat{\boldsymbol{r}}_{-1} = -\hat{\boldsymbol{D}}\hat{\boldsymbol{r}}_{-2}. \tag{4.6}$$

To eliminate dependence of the left-hand side on the unknown vectors $\hat{\boldsymbol{r}}_{-1}$ and $\hat{\boldsymbol{r}}_{-2}$, the left eigenvectors, corresponding to the eigenproblem adjoint to (4.2), may be used. By repeating the arguments used to determine $\hat{\boldsymbol{r}}_0$, these may be expanded as $\hat{\boldsymbol{l}} = \hat{\boldsymbol{l}}_0 + k^{-1}\hat{\boldsymbol{l}}_{-1} + \cdots$ and inferred to satisfy $\hat{\boldsymbol{l}}_0^T\hat{\boldsymbol{D}} = \boldsymbol{0}$ and $\hat{\boldsymbol{l}}_0^T(\hat{\boldsymbol{B}} - \sigma_1\boldsymbol{I}) = \mathrm{i}\hat{\boldsymbol{l}}_{-1}^T\boldsymbol{D}$ (when $\sigma_2 = 0$). For any of the $i$ modes, the dot product of the leading-order left eigenvector $\hat{\boldsymbol{l}}_0$ may be taken with (4.6) and, on rearranging the result, the formula

$$\sigma_0 = \frac{\hat{\boldsymbol{l}}_0 \cdot \hat{\boldsymbol{C}}\hat{\boldsymbol{r}}_0}{\hat{\boldsymbol{l}}_0 \cdot \hat{\boldsymbol{r}}_0} \tag{4.7}$$

is obtained. The corresponding left and right eigenvectors for $\hat{\boldsymbol{B}}_{red}$ are the vectors $\hat{\boldsymbol{l}}_0$, $\hat{\boldsymbol{r}}_0$ with the last $N - i$ entries (which are all zeros) deleted. When $\hat{\boldsymbol{B}}_{red}$ is diagonalisable, these vectors form a biorthonormal set, with the left and right eigenvectors for each mode



https://doi.org/10.1017/jfm.2025.10297 Published online by Cambridge University Press

satisfying $\hat{\boldsymbol{l}}_0 \cdot \hat{\boldsymbol{r}}_0 = 1$, so the $O(1)$ growth rate in (4.7) is well defined. However, if $\hat{\boldsymbol{B}}_{red}$ is not diagonalisable, at least one of its eigenvalues is defective. Therefore, $\sigma_1$ is a repeated eigenvalue associated with one or more Jordan chains of length at least two. Then for the full matrix $\hat{\boldsymbol{B}}$ there are two pairs of corresponding generalised left and right eigenvectors $\hat{\boldsymbol{l}}_{0,1}$, $\hat{\boldsymbol{l}}_{0,2}$ and $\hat{\boldsymbol{r}}_{0,1}$, $\hat{\boldsymbol{r}}_{0,2}$, respectively, satisfying

$$\begin{cases} \hat{\boldsymbol{l}}_{0,1}^T(\hat{\boldsymbol{B}} - \sigma_1 \boldsymbol{I}) = \boldsymbol{0}, \\ \hat{\boldsymbol{l}}_{0,2}^T(\hat{\boldsymbol{B}} - \sigma_1 \boldsymbol{I}) = \hat{\boldsymbol{l}}_{0,1}^T \end{cases} \quad \text{and} \quad \begin{cases} (\hat{\boldsymbol{B}} - \sigma_1 \boldsymbol{I})\hat{\boldsymbol{r}}_{0,1} = \boldsymbol{0}, \\ (\hat{\boldsymbol{B}} - \sigma_1 \boldsymbol{I})\hat{\boldsymbol{r}}_{0,2} = \hat{\boldsymbol{r}}_{0,1}, \end{cases} \tag{4.8a,b}$$

where $\hat{\boldsymbol{r}}_{0,1} \equiv \hat{\boldsymbol{r}}_0$ and $\hat{\boldsymbol{l}}_{0,1} \equiv \hat{\boldsymbol{l}}_0$. In this case, the formula in (4.7) is always singular, since projecting any left eigenvector onto (4.8*b*) shows that $\hat{\boldsymbol{l}}_0 \cdot \hat{\boldsymbol{r}}_0 = 0$. Physically, this singularity can be thought to emerge from a resonance between two or more modes that collapse onto one another when $\hat{\boldsymbol{B}}_{red}$ becomes defective. Examples of this are given in § 4.3.

The failure of (4.7) in these cases suggests the need for an alternative asymptotic expansion. Anticipating growth of some intermediate order between $O(k)$ and $O(1)$, we replace the expansions in (4.3*a*,*b*) with

$$\sigma = -\mathrm{i}\sigma_1 k + \sigma_{1/2} k^{1/2} + \sigma_0 + \cdots, \quad \hat{\boldsymbol{r}} = \hat{\boldsymbol{r}}_{0,1} + k^{-1/2}\hat{\boldsymbol{r}}_{-1/2} + k^{-1}\hat{\boldsymbol{r}}_{-1} + \cdots. \tag{4.9a,b}$$

This leaves the analysis at $O(k)$ unchanged and introduces the following equation at $O(k^{1/2})$:

$$\sigma_{1/2}\hat{\boldsymbol{r}}_{0,1} + \mathrm{i}(\hat{\boldsymbol{B}} - \sigma_1 \boldsymbol{I})\hat{\boldsymbol{r}}_{-1/2} + \hat{\boldsymbol{D}}\hat{\boldsymbol{r}}_{-3/2} = \boldsymbol{0}. \tag{4.10}$$

We project this onto $\hat{\boldsymbol{l}}_{0,2}$ and use (4.8), along with the fact that $\hat{\boldsymbol{l}}_{0,2}$ is orthogonal to the range of $\hat{\boldsymbol{D}}$, to conclude that

$$\sigma_{1/2}\hat{\boldsymbol{l}}_{0,2} \cdot \hat{\boldsymbol{r}}_0 + \hat{\boldsymbol{l}}_{0,1} \cdot \hat{\boldsymbol{r}}_{-1/2} = 0. \tag{4.11}$$

The unknown vector $\hat{\boldsymbol{r}}_{-1/2}$ is eliminated by proceeding to the $O(1)$ equation. With the new expansion, this is

$$\sigma_{1/2}\hat{\boldsymbol{r}}_{-1/2} + \sigma_0\hat{\boldsymbol{r}}_{0,1} + \mathrm{i}(\hat{\boldsymbol{B}} - \sigma_1 \boldsymbol{I})\hat{\boldsymbol{r}}_{-1} - \hat{\boldsymbol{C}}\hat{\boldsymbol{r}}_{0,1} + \hat{\boldsymbol{D}}\hat{\boldsymbol{r}}_{-2} = \boldsymbol{0}. \tag{4.12}$$

Then, we project this onto $\hat{\boldsymbol{l}}_{0,1}$. Since $\hat{\boldsymbol{l}}_{0,1} \cdot \hat{\boldsymbol{r}}_{0,1} = 0$, the term containing $\sigma_0$ vanishes, along with the diffusive term which lies in an orthogonal subspace. After rearranging and using (4.11), we obtain a formula for the $O(k^{1/2})$ part of the growth rate:

$$\sigma_{1/2} = \pm\frac{1+\mathrm{i}}{2}\left(\frac{2\hat{\boldsymbol{l}}_{0,1} \cdot \hat{\boldsymbol{C}}\hat{\boldsymbol{r}}_{0,1}}{\hat{\boldsymbol{l}}_{0,2} \cdot \hat{\boldsymbol{r}}_{0,1}}\right)^{1/2}. \tag{4.13}$$

For Jordan chains of length two, $\hat{\boldsymbol{l}}_{0,2} \cdot \hat{\boldsymbol{r}}_{0,1} = |\hat{\boldsymbol{l}}_{0,2}||\hat{\boldsymbol{r}}_{0,1}| \neq 0$, provided both the left and right vectors correspond to the same Jordan block. Consequently, (4.13) implies that there is a mode such that $\mathrm{Re}(\sigma) \sim k^{1/2}$, provided the source terms in $\hat{\boldsymbol{C}}$ do not interact with the eigenvectors of $\hat{\boldsymbol{B}}$ in a way that causes the numerator to vanish.

Conversely, for longer Jordan chains, the denominator in the (4.13) formula is also guaranteed to be singular. Different asymptotic expansions are needed, depending on the length of the the chain. However, to avoid these further complications, we terminate our analysis here, since cases where three or more modes intersect at high wavenumber are far less commonly encountered.



https://doi.org/10.1017/jfm.2025.10297 Published online by Cambridge University Press

To summarise the analysis above, models up to second order that may be cast in the general form of (3.4) are ill posed as initial-value problems if any of the following conditions are met:

(i) Any eigenvalue of $\hat{\boldsymbol{D}}$ is negative, where $\hat{\boldsymbol{D}}$ denotes a diagonalisation of $\boldsymbol{A}^{-1}\boldsymbol{D}$.

(ii) Any eigenvalue of $\hat{\boldsymbol{B}}_{red}$ is complex, where $\hat{\boldsymbol{B}}_{red}$ denotes the matrix formed by representing $\boldsymbol{A}^{-1}\boldsymbol{B}$ in the basis used to diagonalise $\boldsymbol{A}^{-1}\boldsymbol{D}$ in (i) and deleting each row and column $j$ such that the $j$th diagonal entry of $\hat{\boldsymbol{D}}$ is zero. We refer to $\hat{\boldsymbol{B}}_{red}$ as a 'reduced Jacobian' in later analysis.

(iii) Repeated real eigenvalues of $\hat{\boldsymbol{B}}_{red}$ of algebraic multiplicity 2 share the same left and right eigenvectors $\hat{\boldsymbol{l}}_{0,1}$ and $\hat{\boldsymbol{r}}_{0,1}$ (up to normalisation), and $\hat{\boldsymbol{l}}_{0,1}\cdot\hat{\boldsymbol{C}}_{red}\hat{\boldsymbol{r}}_{0,1}\neq 0$, where $\hat{\boldsymbol{C}}_{red}$ is defined via $\boldsymbol{A}^{-1}\boldsymbol{C}$ in the same way as $\hat{\boldsymbol{B}}_{red}$. (More generally, the expectation following from (4.7) is that repeated real eigenvalues of any algebraic multiplicity $m\geqslant 2$ imply ill posedness if the dimension of their associated eigenspace is strictly less than $m$, but this is not explicitly proven above.)

For the remainder of this section, we apply these steps to different example systems.

### 4.2. *Velocity diffusion in every momentum equation*

Before analysing individual models, we highlight a generic case, which is guaranteed to be well posed. Consider an $n$-phase model, with each phase $i$ characterised by height $H_i$ and velocity $\overline{u_i}$, organised into pairs of mass and momentum equations of the form

$$\frac{\partial H_i}{\partial t}+\frac{\partial}{\partial x}\left(H_i\overline{u_i}\right)=0,\qquad \frac{\partial \overline{u_i}}{\partial t}+F_i(H_1,\overline{u_1},\ldots,H_n,\overline{u_n})=0, \tag{4.14a,b}$$

where the functions $F_i$ contain no dependence on time derivatives or spatial derivatives of first order or higher. To each of the the $j=1,\ldots,n$ momentum equations, add a term of the form $(\partial/\partial x)(\nu_j(\boldsymbol{q})(\partial\overline{u_j}/\partial x))$, where $\nu_j(\boldsymbol{q})$ denotes a general diffusivity coefficient function that stays strictly positive. When casting the linearised problem in matrix form, the equations are ordered so that the mass and momentum equations respectively lie on odd and even rows, as before. The corresponding diffusion matrix is already diagonal, so at any $\boldsymbol{q}=\boldsymbol{q}_0$,

$$\hat{\boldsymbol{D}}=\begin{pmatrix}0 & 0 & \ldots & 0 & 0\\ 0 & \nu_1(\boldsymbol{q}_0) & \ldots & 0 & 0\\ \vdots & \vdots & \ddots & \vdots & \vdots\\ 0 & 0 & \ldots & 0 & 0\\ 0 & 0 & \ldots & 0 & \nu_n(\boldsymbol{q}_0)\end{pmatrix}, \tag{4.15}$$

which is positive semidefinite and damps out growth at high wavenumber for $n$ of the $2n$ stability modes. The reduced Jacobian matrix is simply

$$\hat{\boldsymbol{B}}_{red}=\begin{pmatrix}\overline{u_1} & 0 & \ldots & 0\\ 0 & \overline{u_2} & \ldots & 0\\ \vdots & \vdots & \ddots & \vdots\\ 0 & 0 & \ldots & \overline{u_n}\end{pmatrix}, \tag{4.16}$$



https://doi.org/10.1017/jfm.2025.10297 Published online by Cambridge University Press

which clearly possesses $n$ real eigenvalues and $n$ linearly independent eigenvectors. Therefore, debris-flow models with $\boldsymbol{A} = \boldsymbol{I}$ can always be regularised by adding positive diffusion to every momentum equation.

### 4.3. *Existing models*

#### 4.3.1. *Meng et al. (2022)*

As detailed in § 2.2, in the model of Meng *et al.* (2022), $\boldsymbol{A} = \boldsymbol{I}$ and only diffusion in the fluid phase is included. The equations are (2.17*a*), (2.22*a*), (2.17*c*) and (2.22*b*), rendered dimensionless as described in § 3.1. The diffusion matrix is already diagonal and is given by

$$\hat{\boldsymbol{D}} = \begin{pmatrix} 0 & 0 & 0 & 0 \\ 0 & 0 & 0 & 0 \\ 0 & 0 & 0 & 0 \\ 0 & 0 & 0 & 2\nu_f \end{pmatrix}, \tag{4.17}$$

where $\nu_f \equiv \eta_f/(\rho_f H_f^{(0)} \overline{u_f}^{(0)}) > 0$ is a dimensionless kinematic viscosity coefficient (though it could equally be viewed as an eddy diffusivity if the flow is turbulent). Therefore, the corresponding reduced Jacobian is formed by removing the fourth row and column from the full matrix $\hat{\boldsymbol{B}} = \boldsymbol{B}$, given in (3.6). At $\boldsymbol{q} = \boldsymbol{q}_0$,

$$\hat{\boldsymbol{B}}_{red} = \begin{pmatrix} R_u & R_H & 0 \\ (\gamma + \beta_1)Fr^{-2} & R_u & (\gamma + \beta_2)Fr^{-2} \\ 0 & 0 & 1 \end{pmatrix}. \tag{4.18}$$

Its eigenvalues are

$$\sigma_1 = 1, \; R_u \pm \frac{\sqrt{R_H(\gamma + \beta_1)}}{Fr} \tag{4.19}$$

with corresponding eigenvectors

$$\begin{pmatrix} R_H \\ 1 - R_u \\ \dfrac{(R_u - 1)^2 Fr^2 - R_H(\gamma + \beta_1)}{\gamma + \beta_2} \end{pmatrix}, \quad \begin{pmatrix} R_H \\ \pm\frac{1}{Fr}\sqrt{R_H(\gamma + \beta_1)} \\ 0 \end{pmatrix}. \tag{4.20}$$

Firstly, note that the latter pair of $\sigma_1$ values equal the characteristics for the solids phase of the 'decoupled' problem, given in (3.7*a*,*b*). Hence, all values are expected to be real. However, there is the opportunity for repeated eigenvalues, which occurs when $\sigma_1 = 1$ matches either of the other two growth rates, i.e. when

$$R_u = 1 \pm \frac{1}{Fr}\sqrt{R_H(\gamma + \beta_1)}. \tag{4.21}$$

This is similar, but not equivalent, to the condition for intersecting decoupled characteristics, given previously in (3.11). By substituting (4.21) into (4.20), it may be verified that the corresponding eigenvectors are equal when this condition is satisfied. Consequently, the equations feature an instability with order $k^{1/2}$ growth rate in the high-wavenumber asymptotic limit and are ill posed wherever (4.21) is satisfied.



https://doi.org/10.1017/jfm.2025.10297 Published online by Cambridge University Press

Diffusion of momentum is often also included in shallow models of dry granular flows (e.g. Gray & Edwards 2014; Baker *et al.* 2016). The general argument in § 4.2 implies that adding a diffusive term of the form $(\partial/\partial x)(\nu_s(\partial\overline{u_s}/\partial x))$, where $\nu_s \equiv \nu_s(\boldsymbol{q}_0) > 0$, to the solids momentum equation is sufficient to regularise this model. Moreover, using analogous arguments to those above, it may be verified that diffusive terms in both momentum terms are required, in order to guarantee that the model stays unconditionally well posed.

Specifically, if $\nu_f = 0$, but diffusion in the solids momentum equation is included, then the reduced Jacobian is formed by eliminating the second row and column of $\hat{\boldsymbol{B}}$, to leave

$$\hat{\boldsymbol{B}}_{red} = \begin{pmatrix} R_u & 0 & 0 \\ 0 & 1 & 1 \\ Fr^{-2} & Fr^{-2} & 1 \end{pmatrix}. \tag{4.22}$$

This matrix is defective when

$$R_u = 1 \pm 1/Fr, \tag{4.23}$$

giving rise to a family of $O(k^{1/2})$ instabilities at these points in parameter space, similar to the case where only fluid diffusion is included.

Note that since we used the general form of $\boldsymbol{B}$ from (3.6) to construct the reduced Jacobians, these assessments apply also to the case of adding simple diffusive terms to regularise the models of Pitman & Le (2005), Pelanti *et al.* (2008) and Meyrat *et al.* (2022).

#### 4.3.2. *Pudasaini (2012)*

This model incorporates two diffusive stresses for the fluids phase: a Newtonian component, equivalent to the term used by Meng *et al.* (2022), and a non-Newtonian closure defined in § 2.3. The relevant contributions to the depth-averaged downslope momentum equation are the second-order terms of (2.25). When the model is converted to the quasilinear form that was used for the local analysis, the fluid momentum equation is non-dimensionalised (as per § 3.1) and divided through by $\rho_f H_f$, and the diffusive terms become

$$\frac{2\nu_f}{H_f}\frac{\partial}{\partial x}\left(H_f\frac{\partial\overline{u_f}}{\partial x}\right) + \frac{2\nu_f\mathcal{N}}{H_f}\frac{\partial}{\partial x}\left[H_f(\overline{u_s}-\overline{u_f})\frac{\partial}{\partial x}\left(\frac{H_s}{H_s+H_f}\right)\right]. \tag{4.24}$$

The parameter $\mathcal{N} = \overline{\mathcal{A}}/\overline{\varphi_f}$ is a ratio of the effective diffusion coefficients for the Newtonian and non-Newtonian parts (see (2.25)) and is assumed to be constant by Pudasaini (2012).

After linearising around $\boldsymbol{q} = \boldsymbol{q}_0 = (R_H,\, R_u,\, 1,\, 1)^T$, the diffusion matrix becomes

$$\boldsymbol{D} = 2\nu_f \begin{pmatrix} 0 & 0 & 0 & 0 \\ 0 & 0 & 0 & 0 \\ 0 & 0 & 0 & 0 \\ \dfrac{\mathcal{N}(R_u-1)}{(1+R_H)^2} & 0 & \dfrac{\mathcal{N}R_H(1-R_u)}{(1+R_H)^2} & 1 \end{pmatrix}. \tag{4.25}$$



https://doi.org/10.1017/jfm.2025.10297 Published online by Cambridge University Press

The matrices $\boldsymbol{A}$ and $\boldsymbol{B}$ were given previously, in (3.12) and (3.13), respectively. The basis change matrix

$$\boldsymbol{P}=\begin{pmatrix} 1 & 0 & 0 & 0 \\ 0 & 1 & 0 & \gamma\overline{C} \\ 0 & 0 & 1 & 0 \\ \dfrac{\mathcal{N}(1-R_u)}{(1+R_H)^2} & 0 & \dfrac{\mathcal{N}R_H(R_u-1)}{(1+R_H)^2} & \gamma\overline{C}+1 \end{pmatrix} \tag{4.26}$$

diagonalises $\boldsymbol{A}^{-1}\boldsymbol{D}$, so that $\hat{\boldsymbol{D}}=\boldsymbol{P}^{-1}\boldsymbol{A}^{-1}\boldsymbol{D}\boldsymbol{P}$ is the matrix of all zeros, save for its only eigenvalue $\sigma_2$, located on the bottom right entry:

$$D_{44}=\sigma_2=\frac{2v_f(\gamma\overline{C}+1)}{1+\overline{C}(\gamma+R_H)}. \tag{4.27}$$

Since $\sigma_2>0$, there is no blow-up at $O(k^2)$ and it remains to check the properties of $\hat{\boldsymbol{B}}_{red}$, which is formed by removing the fourth row and column of $\boldsymbol{P}^{-1}\boldsymbol{A}^{-1}\boldsymbol{B}\boldsymbol{P}$.

In the general case, analytical expressions for this matrix are cumbersome and it is better to compute its eigenvalues numerically. However, two limiting cases are tractable. Firstly, when the non-Newtonian viscosity is not included, $\mathcal{N}=0$ and the reduced Jacobian is

$$\hat{\boldsymbol{B}}_{red}=\begin{pmatrix} R_u & R_H & 0 \\ \dfrac{1}{\gamma\overline{C}+1}\left[\dfrac{\gamma+\beta_1}{Fr^2}+\dfrac{\overline{C}(R_u-1)}{R_H}\right] & R_u+\dfrac{\gamma\overline{C}}{\gamma\overline{C}+1} & \dfrac{\gamma+\beta_2}{(\gamma\overline{C}+1)Fr^2} \\ 0 & 0 & 1 \end{pmatrix}. \tag{4.28}$$

The eigenvalues $\sigma_1$ of this matrix are

$$\sigma_1=1,\ R_u+\frac{1}{\gamma\overline{C}+1}\left(\frac{\gamma\overline{C}}{2}\pm\frac{\sqrt{\Delta}}{Fr}\right), \tag{4.29}$$

where

$$\Delta=(\gamma\overline{C}+1)\left[Fr^2\gamma\overline{C}(R_u-1)+(\gamma+\beta_1)R_H\right]+\left(\frac{Fr\gamma\overline{C}}{2}\right)^2. \tag{4.30}$$

The latter pair are complex conjugate if and only if $\Delta<0$. Rearranging this inequality leads to

$$R_u-1<-\frac{\gamma\overline{C}}{4(\gamma\overline{C}+1)}-\frac{R_H(\gamma+\beta_1)}{\gamma\overline{C}Fr^2}. \tag{4.31}$$

This describes a region of complex eigenvalues that is constrained to lie within $R_u<1$. Note that in the $\overline{C}\to 0$ limit, this region entirely recedes and inequality (4.31) is never satisfied. In addition to these complex eigenvalues, there is the opportunity for $O(k^{1/2})$ blow-up if $\hat{\boldsymbol{B}}_{red}$ is defective, which can happen if $\sigma_1=1$ intersects with either of the other two eigenvalues in (4.29). The condition for this simplifies to

$$R_u=1\pm\frac{1}{Fr}\sqrt{\frac{R_H(\gamma+\beta_1)}{\gamma\overline{C}+1}}, \tag{4.32}$$



https://doi.org/10.1017/jfm.2025.10297 Published online by Cambridge University Press

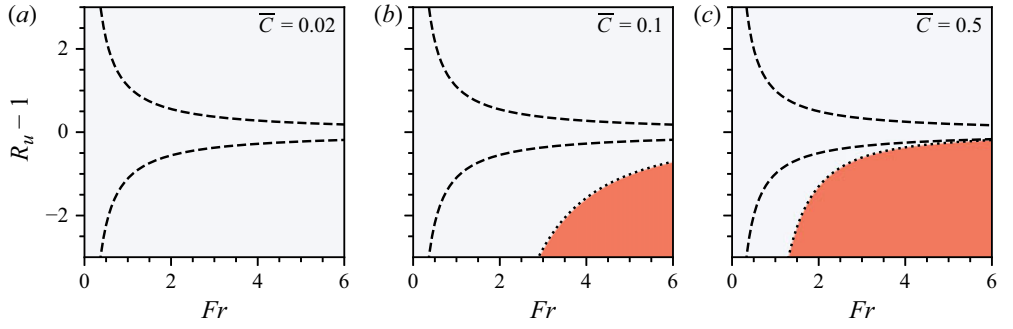



Figure 7. Regions where the reduced Jacobian for the model of Pudasaini (2012) with diffusive terms possesses complex eigenvalues (red shading), for $R_H = 1$, $\gamma = 0.5$, $\mathcal{N} = 0$ and $\overline{C} =$ (*a*) 0.02, (*b*) 0.1 and (*c*) 0.5. The boundaries of these regions are given analytically by inequality (4.31) (dotted black). Along the black dashed lines, given by (4.32), the reduced Jacobian is defective. The model is ill posed as an initial-value problem for flow states that pass through either the dashed line or the red region.

which generalises (4.21) for cases where $\overline{C} \geqslant 0$. It may be separately verified that only one eigenvector corresponding to $\sigma_1 = 1$ exists when $R_u$ satisfies (4.32), implying that $\hat{\boldsymbol{B}}_{red}$ is defective here.

In figure 7, we show the regions where the model is ill posed for $\mathcal{N} = 0$, $\overline{C} =$ 0.02, 0.1 and 0.5 and the same illustrative parameters used in figure 4(*a*). Dashed curves show the lines given by (4.32). The ill-posed region that emerges at low $R_u$ values via inequality (4.31), whose border is given by the dotted line, may be compared with similar regions present in the problem without diffusion, plotted in figure 4.

If instead $\mathcal{N} > 0$ and the limit of vanishing added mass $\overline{C} \to 0$ is taken, then

$$\hat{\boldsymbol{B}}_{red} = \begin{pmatrix} R_u & R_H & 0 \\ (\gamma+\beta_1)Fr^{-2} & R_u & (\gamma+\beta_2)Fr^{-2} \\ \dfrac{\mathcal{N}(1-R_u)}{(1+R_H)^2} & 0 & 1+\dfrac{\mathcal{N}R_H(R_u-1)}{(1+R_H)^2} \end{pmatrix}. \tag{4.33}$$

Note that this is a generalisation of the reduced Jacobian in (4.18). When the non-Newtonian terms are included, $\mathcal{N}$ is expected to be a large number compared with the other parameters (Pudasaini (2012) uses $\mathcal{N} = 5000$). By solving for roots of the characteristic polynomial via series expansion, when $\mathcal{N} \gg 1$, the eigenvalues of $\hat{\boldsymbol{B}}_{red}$ may be obtained:

$$\sigma_1 = \frac{(R_u-1)R_H}{(1+R_H)^2}\mathcal{N} + 1 + O(\mathcal{N}^{-1}), \quad \pm\frac{1}{Fr}\sqrt{(\gamma+\beta_1)R_H+\gamma+\beta_2} + O(\mathcal{N}^{-1}). \tag{4.34}$$

These expressions are real-valued and remain so in the limit. However, either of the second and third branches merges with the first when

$$R_u = 1 \pm \frac{(1+R_H)^2}{FrR_H\mathcal{N}}\sqrt{(\gamma+\beta_1)R_H+\gamma+\beta_2} + O(\mathcal{N}^{-2}). \tag{4.35}$$

As we have seen previously, the merging of branches can give rise to complex eigenvalues. In this case, the merger originates in the limit $\mathcal{N} \to \infty$. For large but finite $\mathcal{N}$, we compute the eigenvalues of $\hat{\boldsymbol{B}}_{red}$ numerically and summarise their type in figure 8. The two parametric lines given in (4.35) are flanked by bands where $\sigma_1$ takes complex



https://doi.org/10.1017/jfm.2025.10297 Published online by Cambridge University Press

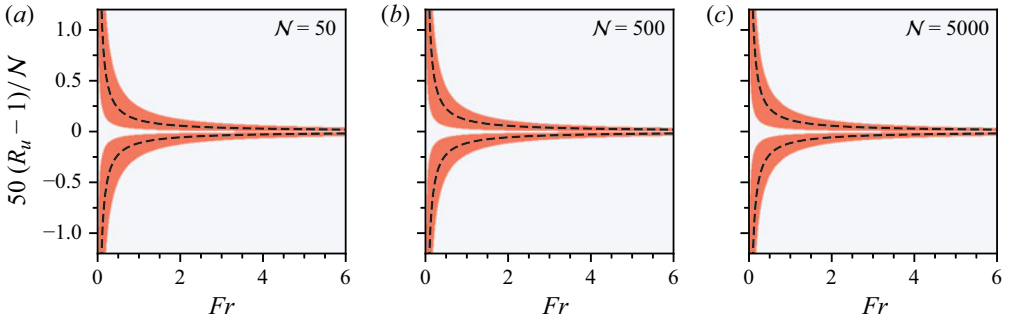



Figure 8. Regions where the model of Pudasaini (2012) with diffusive terms is ill posed as an initial-value problem (red shading), for $R_H = 1$, $\gamma = 0.5$, $\overline{C} = 0$ and high values of the ratio $\mathcal{N}$ between non-Newtonian and Newtonian diffusion coefficients: $\mathcal{N} = (a)$ 50, $(b)$ 500 and $(c)$ 5000. Note that each vertical axis is scaled with respect to $50/\mathcal{N}$ and that the shaded regions are near identical under this rescaling. Asymptotic expansions for the eigenvalues at high $\mathcal{N}$ intersect along the black dashed lines, whose formulae are given in (4.35).

values. Furthermore, the shape of these bands is self-similar in the asymptotic high-$\mathcal{N}$ regime.

#### 4.3.3. *Pudasaini & Mergili (2019)*

To conclude this section, we touch upon the three-phase model of Pudasaini & Mergili (2019), which was introduced in § 3.2. It was shown previously that omitting the diffusive terms in this model can lead to ill-posed initial-value problems. However, it remains to be seen whether including the terms can eliminate this issue. As before, we neglect the complications of the added mass effect, though as we have just seen, this can be analysed using the same methods.

Diffusion of momentum in the Pudasaini & Mergili (2019) model appears in the equations for both fluid phases (which are labelled 2 and 3 in § 3.2). Each contains a Newtonian and non-Newtonian component similar to the terms in (4.24) for the Pudasaini (2012) system. The diffusion matrix $\boldsymbol{D}$ for the non-dimensionalised and linearised model equations is given explicitly in Appendix C. Due to the non-Newtonian terms, it has off-diagonal entries. It possesses two non-zero eigenvalues, which are $2\nu_2 > 0$ and $2\nu_3 > 0$, where $\nu_2$ and $\nu_3$ are the Newtonian diffusion coefficients associated with the second and third phases. A suitable basis change matrix $\boldsymbol{P}$ that diagonalises $\boldsymbol{D}$ was determined using computational algebra and is also specified in Appendix C. This allows us to form the reduced Jacobian (a $4 \times 4$ matrix in this case) numerically and compute its eigenvalues.

Since there are five independent dimensionless variables ($R_{H_1}$, $R_{H_2}$, $R_{u_1}$, $R_{u_2}$, $Fr$) that specify a particular state (in addition to several fixed model parameters), we do not attempt an exhaustive study. Instead, we fix $R_{H_1} = 1$ and investigate the effect of introducing the intermediate fluid phase by increasing $R_{H_2}$ from zero. Guided by our analysis in § 3.2, we shift $R_{u_2}$ slightly away from unity, setting $R_{u_2} = 1.01$, to allow for richer interactions between the phases. Figure 9 shows the results of these computations, using illustrative model parameters, given in Appendix C. These parameters were selected to match our choices for computations relating to the Pudasaini (2012) model with $\mathcal{N} = 5000$ (§ 4.3.2), so that when $R_{H_2} \to 0$, the system collapses to the this two-phase case. When $R_{H_2} = 10^{-3}$ (figure 9*a*), there are two bands where the reduced Jacobian features a pair of complex eigenvalues, either side of $R_{u_1} = 1$. As expected, these closely match the corresponding regions plotted in figure 8(*c*). However, the reflection symmetry of these bands about $R_{u_1} = 1$ is broken for any $R_{H_2} > 0$. This becomes apparent at higher $R_{H_2}$



https://doi.org/10.1017/jfm.2025.10297 Published online by Cambridge University Press

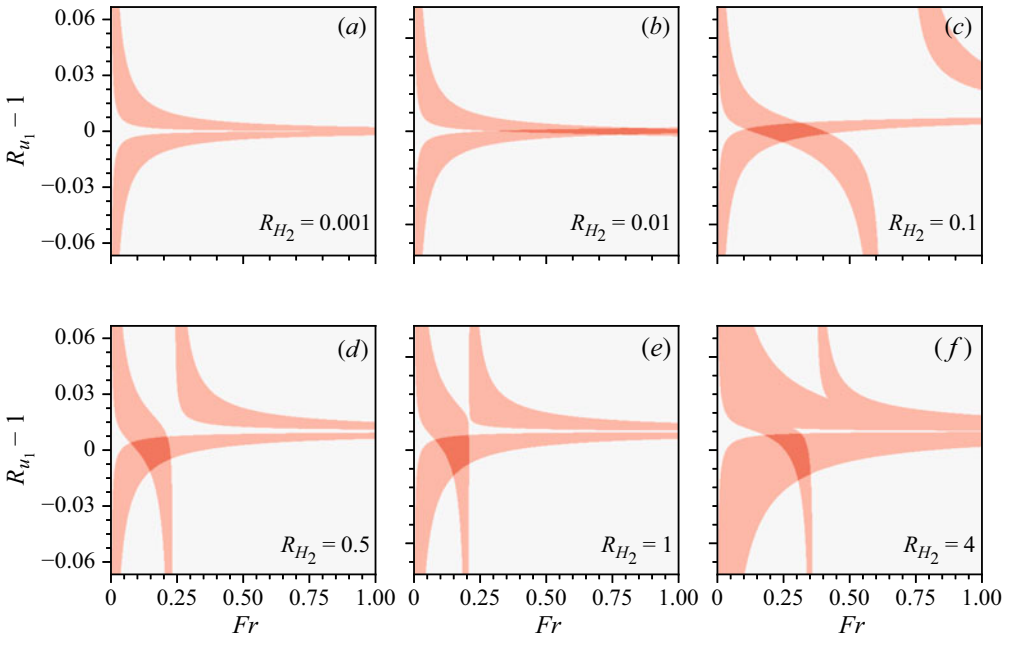



Figure 9. Illustrative computations of the eigenvalues of $\hat{\boldsymbol{B}}_{red}$ for the model of Pudasaini & Mergili (2019), with $R_{H_1} = 1$ and $R_{u_2} = 1.01$. In regions shaded pink, the model possesses a single pair of complex eigenvalues, while red shading covers areas where two complex pairs were found. Elsewhere, all eigenvalues are real. The parameters for these computations are given in Appendix C.

values. Figures 9(*b*) and 9(*c*) show the cases $R_{H_2} = 0.01$ and 0.1, respectively. The upper band drops below $R_{u_1} < 1$ and overlaps the lower band, with the Froude numbers at which this occurs decreasing as $R_{H_2}$ increases. Where the bands overlap, there are two pairs of complex eigenvalues. Additionally, a second upper band appears at higher $Fr$ and draws towards lower $Fr$ as $R_{H_2}$ increases to 0.5 and 1, in figures 9(*d*) and 9(*e*), respectively. In the final plot (figure 9*f*), at $R_{H_2} = 4$, the two upper bands have merged, though in this case the merger does not double the number of complex eigenvalues present.

Other choices for the flow variables lead to plots that are similar to figure 9, at least in the sense that they are constructed from complicated tangles of complex eigenvalue regions. While it may be possible to make sense of these diagrams in detail, this is perhaps beside the point. It is clear, even from this cursory investigation, that this three-phase model suffers from the same issues as the two-phase models.

## 5. Discussion

We have seen that depth-averaged debris-flow models with mass and momentum equations for more than one phase lead to initial-value problems that are only conditionally well posed. In particular, they are overcome by catastrophic instabilities if their flow fields stray into certain regions of parameter space. This limits their applicability to cases where solutions provably avoid these regions. For example, travelling-wave solutions, such as those constructed by Meng *et al.* (2022) in their model, are mathematically constrained to have equal depth-averaged velocities for both phases ($R_u = 1$) – a case which we have seen is guaranteed to be well posed for the simplest two-phase models. However, since

https://doi.org/10.1017/jfm.2025.10297 Published online by Cambridge University Press

the ill-posed regions lie well within physically accessible regimes, no such guarantee can be made *a priori* for simulations of real flows over complex topographies. This calls into question the reliability of computational results obtained with multi-phase models in prior studies over the past two decades. Furthermore, it strongly suggests that these systems should not be used in scientific applications such as hazards assessment, since any numerical 'solutions' whose flow fields stray into an ill-posed region become impossible to converge to values that faithfully approximate the underlying partial differential equations.

A common observation in our analysis has been that adding physical detail to a debris-flow model can exacerbate the problem of ill posedness by increasing the opportunities for unwelcome resonant interactions between flow fields. Therefore, for operational purposes, it may be wisest for practitioners to adopt a philosophy of favouring models that are 'as simple as possible (but no simpler)'. In most cases, this will mean depth-averaged systems that provide a single bulk momentum equation for the flowing mixture. Such systems can capture most of the important debris-flow physics and available models either inherit well posedness from the classical shallow-water equations, or have independently been shown to be strictly hyperbolic, such as the models of Kowalski & McElwaine (2013) and George & Iverson (2014). However, simplicity comes with the potential risk of missing or mispredicting key phenomena, such as the longitudinal separation of the phases over the length of a debris flow. For situations where a fully multi-phase description is absolutely necessary, careful model development is needed to resolve the issues raised herein.

The analysis of § 4.1, which provides a general procedure for identifying ill posedness in initial-value problems of up to second order in their spatial derivatives, should prove useful in this regard. This may be applied either numerically or (ideally) analytically, to assess particular models and indicate possible ways to regularise them. One option that we have highlighted is to add diffusive terms. It is surely reasonable to justify the presence of momentum diffusion in any phase of a debris flow, over a suitable range of scales and doing so provides a potentially straightforward way to avoid model pathologies. However, while diffusion might be expected to automatically regularise the system, we show in § 4.3 that this is not the case for the existing models analysed herein. Moreover, the appropriate size of the diffusion coefficients in each case may not be clear in advance and careful work is needed in order to formulate these terms rigorously for particular flows. Nevertheless, ill posedness is provably avoided for the natural case of a diagonal diffusion operator with strictly positive entries for each momentum equation and zeros elsewhere. Alternatively, it may be possible to benefit from the existing research on numerical methods for the multi-layer shallow-water equations (Castro Díaz *et al.* 2023) to design schemes that avoid non-hyperbolic regimes without diffusive terms, bearing in mind that any such approach would need to be physically justified for debris flows.

A deeper question remains. To what extent does the presence of ill posedness in these models signify the existence of underlying physical instabilities? The removal of the mathematical pathology does not necessarily imply the removal of the associated linear instability. In particular, regularising a model by diffusively damping out growth at high wavenumbers can leave larger scales unaffected and susceptible to the same dramatic instability that gave rise to ill posedness (Baker *et al.* 2016; Langham *et al.* 2021). The finger-like structures observed in granular flow fronts are a prime example of this. Depth-averaged equations for the dynamics of segregated bidisperse grains suffer from ill posedness of the $O(k^{1/2})$ kind, arising from repeated real characteristics (Woodhouse *et al.* 2012). Nevertheless, the inclusion of a physically motivated diffusive



https://doi.org/10.1017/jfm.2025.10297 Published online by Cambridge University Press

term regularises the model and sets the preferred fingering width (Baker *et al.* 2016). Therefore, at least in this case, ill posedness signposts the existence of an underlying physical instability – one that can be correctly captured following improvements to the model. This is more generally to be expected, since a properly formulated shallow-layer model that undergoes a Hadamard instability must be regularised with physics that are only non-negligible over the short length scales where the instability becomes acute. (Otherwise those terms would have to be present in the original model formulation).

Given the difficulties in conducting experiments and observations of debris flows, it remains to be seen what kind of instability this analysis might be pointing towards. Free-surface instabilities that give rise to large-amplitude 'roll waves' and related phenomena are already known to occur in debris flows (Zanuttigh & Lamberti 2007; Schöffl *et al.* 2023; Chen *et al.* 2024). However, in these cases, the instability mechanism emerges from interactions between gravitational forcing and frictional resistance from basal stresses (Trowbridge 1987). The instabilities that we have considered in this paper are independent of these effects. Instead, they arise from the coupling between the phases provided by buoyancy. Consequently, they seem more likely to be related to interior instabilities found in multi-layered fluid flows such as the Kelvin–Helmholtz mechanism (Castro *et al.* 2001). In a well-mixed flow of fluid and grains, the phenomenology of such an instability would need to be quite different. Nevertheless, perhaps it will turn out that the high-frequency resonance between the two phases is ultimately resolved similarly to the case of mixing between fluid layers. That is, through the generation of internal vortices that dissipate energy and act to reduce the velocity difference between the phases, thereby driving the modelled flow away from non-hyperbolic regions. Unravelling these issues could be an interesting challenge for future study.

**Supplementary movies.** Supplementary movies are available at https://doi.org/10.1017/jfm.2025.10297.

**Acknowledgements.** J.L. acknowledges fruitful discussions with A.J. Hogg over the course of this work.

**Funding.** This research was supported by funding from National Environment Research Council (NERC) grants NE/X00029X/1 and NE/X013936/1. X.M. is grateful for the support of China NFSC grant no. 12272074 and the Liaoning Revitalization Talents Program (XLYC2203149). J.M.N.T.G. was supported by a Royal Society Wolfson Research Merit Award (WM150058) and an EPSRC Established Career Fellowship (EP/M022447/1).

**Declaration of interests.** The authors report no conflict of interest.

## Appendix A. Details of the figure 1 numerical simulations

The data for the illustrative simulation in figure 1 were obtained by numerically integrating the Meng *et al.* (2022) model equations for oversaturated debris flows (2.17*a*), (2.22*a*) for the solids phase and (2.17*c*), (2.22*b*) for the fluid phase), using the finite-volume scheme of Kurganov & Tadmor (2000) in combination with the technique of Kurganov & Petrova (2009) to handle non-conservative product terms. Though the source terms in (2.22*a*) and (2.22*b*) do not affect the presence of the catastrophic instabilities in the model, they must be specified to simulate the equations. The following closures were employed:

$$S_s = -g^x - (1-\gamma) g^z \mu_b \frac{\overline{u_s}}{|\overline{u_s}|} - \frac{C_d}{\rho_s \varphi_c}(\overline{u_s} - \overline{u_f}), \tag{A1a}$$

$$S_f = -g^x - C_w \frac{\overline{u_f}|\overline{u_f}|}{H_f} - \frac{C_d}{\rho_f \varphi_c}\frac{H_s}{H_f}(\overline{u_f} - \overline{u_s}), \tag{A1b}$$



https://doi.org/10.1017/jfm.2025.10297 Published online by Cambridge University Press

where $\mu_b$ and $C_w$ are dimensionless coefficients and $C_d$ is a dimensional Darcy drag coefficient modelled by $C_d = 180\eta_f\varphi_c^2/[d^2(1-\varphi_c)]$, with $\eta_f$ denoting the dynamic viscosity of the fluid and $d$ a characteristic solids diameter. These capture the essential competition between downslope gravitational acceleration $g^x$, basal drag and interphase (Darcy) drag in these systems. The $\mu_b$ coefficient for the solids phase is dynamically set by a granular friction law (Pouliquen & Forterre 2002; Jop, Forterre & Pouliquen 2005):

$$\mu_b = \mu_1 + \frac{\mu_2 - \mu_1}{1 + I_0/I}, \quad \text{where} \quad I = \frac{5|\overline{u_s}|d\varphi_c^{3/2}}{2(g^z\varphi_c H_s^3)^{1/2}} \tag{A2}$$

is a so-called 'inertial number' for the grains.

The source term parameter values used were: $g^x = -g\sin(18.5°)$, $g^z = g\cos(18.5°)$, where $g = 9.8\,\mathrm{m\,s^{-2}}$, $\rho_s = 1400\,\mathrm{kg\,m^{-3}}$, $\rho_f = 1000\,\mathrm{kg\,m^{-3}}$ (implying $\gamma = 1/1.4$ ($\approx 0.7$)), $\eta_f = 10^{-3}\,\mathrm{kg\,m^{-1}\,s^{-1}}$, $\mu_1 = \tan(22.5°)$, $\mu_2 = \tan(30.1°)$, $d = 8\times10^{-3}$ m, $\varphi_c = 0.5$, $I_0 = 9/(44\sqrt{\varphi_c})$ ($\approx 0.3$) and $C_w = 0.01$. Additionally, diffusion of fluid momentum was neglected, i.e. $\nu_f = 0$ (though note that dynamic viscosity $\eta_f$ retains a non-zero value for the purposes of the Darcy drag closure). Simulations were conducted in a domain of length $L = 0.3$ m with periodic boundary conditions enforced for all fields at $x = 0$ m $\equiv 0.2$ m and three numerical grid spacings $\Delta x = 5\times10^{-4}$ m, $5\times10^{-5}$ m and $5\times10^{-6}$ m. In each case the initial condition used was a steady uniform flow in an ill-posed regime of the model. Such states occur when the source terms vanish, implying flow at equilibrium, with $S_s = S_f = 0$. Specifically, $h_s = 0.0945794565$ m, $\overline{u_s} = 6.5195983137\,\mathrm{m\,s^{-1}}$, $h_f = 0.1176076626$ m, $\overline{u_f} = 5.711201893\,\mathrm{m\,s^{-1}}$ were set at $t = 0$. The equivalent partial depths $H_s$, $H_f$ are obtained via the transformations in (2.21). To 3 s.f., the corresponding dimensionless field variables are $R_H = 0.673$, $R_u = 1.14$ and $Fr = 7.06$. Additionally, a small disturbance was given to this initial condition. Specifically, each field $q$ was initialised at $t = 0$, to the real part of

$$q_0\left[1 + \frac{\epsilon}{||\boldsymbol{\xi}||}\sum_{n=1}^{n=N} A_n \exp\left(\mathrm{i}2\pi nx/L\right)\right], \tag{A3}$$

where $q_0$ denotes the corresponding steady uniform flow value for the field, $\epsilon = 10^{-6}$, $N = L/\Delta x$ is the number of simulation grid cells and $\boldsymbol{\xi}$ is a vector of complex-valued random amplitudes uniformly distributed within in the unit circle, with norm $||\boldsymbol{\xi}|| = (|\xi_1|^2 + \ldots + |\xi_N|^2)^{1/2}$.

## Appendix B. Table of notation

To ease comparison between different models and our analysis, table 1 lists the main symbols used in the paper, alongside the equivalent quantities in Pitman & Le (2005), Pudasaini (2012) and Meng *et al.* (2022) using the original authors' notation. Not all the symbols can be directly translated, either because some terms only appear in a subset of models or due to conceptual differences in approach. For example, instead of the quantities that we term the 'effective stresses', some authors define stress tensors that incorporate part of the buoyancy effect (which itself is not uniquely defined in this context; see Jackson (2000)). These differences in bookkeeping, though conceptually meaningful, do not ultimately lead to incompatible physical descriptions once the models are carefully depth-averaged.



https://doi.org/10.1017/jfm.2025.10297 Published online by Cambridge University Press

| | This paper | Pitman & Le (2005) | Pudasaini (2012) | Meng *et al.* (2022) |
|---|---|---|---|---|
| Velocity | $\boldsymbol{u}_s, \boldsymbol{u}_f$ | $\boldsymbol{v}, \boldsymbol{u}$ | $\boldsymbol{u}_s, \boldsymbol{u}_f$ | $\boldsymbol{u}^g, \boldsymbol{u}^w$ |
| Density | $\rho_s, \rho_f$ | $\rho^s, \rho^f$ | $\rho_s, \rho_f$ | $\rho^{g\star}, \rho^{w\star}$ |
| Density ratio $(\rho_f/\rho_s)$ | $\gamma$ | — | $\gamma$ | $\gamma$ |
| Volume fraction | $\varphi_s, \varphi_f$ | $\varphi, 1-\varphi$ | $\alpha_s, \alpha_f$ | $\phi^g, \phi^w$ |
| Constant solids volume fraction | $\varphi_c$ | — | — | $\phi^c$ |
| Effective solids stress | $\boldsymbol{\sigma}_s$ | $-\boldsymbol{T}^s$ | $\alpha_s(p\boldsymbol{I}-\boldsymbol{T}_s)$ | $-\boldsymbol{\sigma}^e$ |
| Effective fluid stress | $\boldsymbol{\sigma}_f$ | $-\boldsymbol{T}^f$ | $-p\boldsymbol{I}+\alpha_f\boldsymbol{\tau}_f$ | $-p^{w\star}\boldsymbol{I}+\boldsymbol{\tau}^w$ |
| Pore fluid pressure | $p$ | — | $p$ | $p^{w\star}$ |
| Total interphase force | $\boldsymbol{f}_s, \boldsymbol{f}_f$ | — | — | — |
| Non-buoyant interphase force | $\boldsymbol{d}_s, \boldsymbol{d}_f$ | $\boldsymbol{f}, -\boldsymbol{f}$ | $\boldsymbol{M}_s, \boldsymbol{M}_f$ | — |
| Gravity vector | $-\boldsymbol{g}$ | $\boldsymbol{g}$ | $\boldsymbol{f}$ | $\boldsymbol{g}$ |
| Total flow depth | $h$ | $\hat{h}$ | $h$ | $h^w$ |
| Partial depth | $H_s, H_f$ | $\overline{\varphi}\hat{h}, (1-\overline{\varphi})\hat{h}$ | $\overline{\alpha_s}h, \overline{\alpha_f}h$ | $\varphi_c h^g$, $h^w-\varphi_c h^g$ |
| Solid/fluid layer depth | $h_s, h_f$ | — | — | $h^g, h^w$ |
| Added mass coefficient | $C$ | — | $C_{VM}$ | — |
| Earth pressure coefficient | $K$ | $\alpha_{xx}$ | $K_x$ | 1 |
| Dynamic fluid viscosity | $\eta_f$ | — | $\eta_f$ | $\eta^w$ |
| Non-Newtonian coefficient | $\mathcal{A}$ | — | $\mathcal{A}$ | — |

Table 1. Comparison of notation for the main two-phase models considered herein. Where no direct analogue of a quantity exists in a given article, we either derive it in the authors' original notation or leave the entry blank. Pairs of quantities refer to solid- and fluid-phase components, respectively. In some cases, we retain hats and overbars that are eventually dropped for brevity in the original articles. As in the main text, the Meng *et al.* (2022) model is assumed to be in its oversaturated configuration.

## Appendix C. Pudasaini & Mergili (2019) coefficient matrices

The analyses of §§ 3.2 and 4.3.3 investigate the eigenstructure of the frozen coefficient problem (3.5) for the model of Pudasaini & Mergili (2019). The underlying model equations are lengthy and fully specified in the original paper. To obtain the relevant matrices for our analysis, the same essential steps are followed as for the two-phase systems. The original equations in conservative form are rewritten in the quasilinear form of (3.4) and non-dimensionalised with respect to the height and velocity of third (fluid) phase, as described in the text around (3.17*a–d*). Then, the coefficients are frozen around a base state given by $H_1 = R_{H_1}$, $\overline{u_1} = R_{u_1}$, $H_2 = R_{H_2}$, $\overline{u_2} = R_{u_2}$, $H_3 = \overline{u_3} = 1$. Finally, the added mass coefficients that appear in the model are assumed to be zero, implying that $\boldsymbol{A} = \boldsymbol{I}$. The Jacobian matrix $\boldsymbol{B}$ is constructed in § 3.2, by evaluating (3.14) and substituting the particular closures for this model, which are given in (3.19*a*, *b*). Since it is not relevant for our analysis, there is no need to specify the source matrix $\boldsymbol{C}$.

Newtonian and non-Newtonian stresses, analogous to those in (4.24), are included for both the fluid phases 2 and 3. This means there are two 'kinematic' viscosities, $\nu_2$ and $\nu_3$, respectively, for the Newtonian stresses, which we render dimensionless with respect to $H_3^{(0)}\overline{u_3}^{(0)}$. Furthermore, a single downslope non-Newtonian diffusive term is proposed for phase 2, while two such terms appear in the momentum equation for phase 3 (Pudasaini & Mergili 2019). This introduces three further parameters $\mathcal{N}_{21}, \mathcal{N}_{31}, \mathcal{N}_{32}$, which are defined similarly to the parameter $\mathcal{N}$ of § 4.3.2, as ratios between non-Newtonian and Newtonian diffusion coefficients. The non-zero entries $D_{ij}$ of the diffusion matrix $\boldsymbol{D}$ are given by



https://doi.org/10.1017/jfm.2025.10297 Published online by Cambridge University Press

$$D_{41} = 2\nu_2 \mathcal{N}_{21} \frac{(R_{u_1} - R_{u_2})(1 + R_{H_2})}{(1 + R_{H_1} + R_{H_2})^2}, \tag{C1a}$$

$$D_{43} = D_{45} = 2\nu_2 \mathcal{N}_{21} \frac{(R_{u_2} - R_{u_1})R_{H_1}}{(1 + R_{H_1} + R_{H_2})^2}, \quad D_{44} = 2\nu_2, \tag{C1b,c}$$

$$D_{61} = \frac{2\nu_3}{(1 + R_{H_1} + R_{H_2})^2} \left[\mathcal{N}_{31}(R_{u_1} - 1)(1 + R_{H_2}) + \mathcal{N}_{32}(1 - R_{u_2})R_{H_2}\right], \tag{C1d}$$

$$D_{63} = \frac{2\nu_3}{(1 + R_{H_1} + R_{H_2})^2} \left[\mathcal{N}_{31}(1 - R_{u_1})R_{H_1} + \mathcal{N}_{32}(R_{u_2} - 1)(1 + R_{H_1})\right], \tag{C1e}$$

$$D_{65} = \frac{2\nu_3}{(1 + R_{H_1} + R_{H_2})^2} \left[\mathcal{N}_{31}(1 - R_{u_1})R_{H_1} + \mathcal{N}_{32}(1 - R_{u_2})R_{H_2}\right], \quad D_{66} = 2\nu_3. \tag{C1f,g}$$

A convenient basis change matrix $\boldsymbol{P}$ that diagonalises $\boldsymbol{D}$ is given by the matrix whose only non-zero entries are

$$P_{41} = -\frac{\mathcal{N}_{21}(1 + R_{H_2})(R_{u_1} - R_{u_2})}{(1 + R_{H_1} + R_{H_2})^2}, \quad P_{43} = P_{45} = \frac{\mathcal{N}_{21}(R_{u_1} - R_{u_2})R_{H_1}}{(1 + R_{H_1} + R_{H_2})^2}, \tag{C2a,b}$$

$$P_{61} = \frac{-\mathcal{N}_{31}(R_{u_1} - 1)(1 + R_{H_2}) + \mathcal{N}_{32}(R_{u_2} - 1)R_{H_2}}{(1 + R_{H_1} + R_{H_2})^2}, \tag{C2c}$$

$$P_{63} = \frac{\mathcal{N}_{31}(R_{u_1} - 1)R_{H_1} - \mathcal{N}_{32}(R_{u_2} - 1)(1 + R_{H_1})}{(1 + R_{H_1} + R_{H_2})^2}, \tag{C2d}$$

$$P_{65} = \frac{\mathcal{N}_{31}(R_{u_1} - 1)R_{H_1} + \mathcal{N}_{32}(R_{u_2} - 1)R_{H_2}}{(1 + R_{H_1} + R_{H_2})^2} \tag{C2e}$$

and $P_{ii} = 1$ for all $i = 1, \ldots, 6$. This matrix is constructed so that the non-zero entries of $\hat{\boldsymbol{D}} = \boldsymbol{P}^{-1}\boldsymbol{D}\boldsymbol{P}$ are $D_{55} = 2\nu_2$ and $D_{66} = 2\nu_3$. Consequently, the reduced Jacobian $\hat{\boldsymbol{B}}_{red}$ is formed by deleting rows and columns 5 and 6 of $\boldsymbol{P}^{-1}\boldsymbol{B}\boldsymbol{P}$. Its eigenvalues are computed numerically in figure 9 for various flow states, using the following illustrative model parameter values: $\gamma_1 = \gamma_2 = 0.5$, $K = 1$ and $\mathcal{N}_{21} = \mathcal{N}_{31} = \mathcal{N}_{32} = 5000$. Note that since $\nu_2$ and $\nu_3$ do not appear in $\boldsymbol{P}$, these values do not need to be specified to reproduce figure 9.

## References


Abgrall, R. & Karni, S. 2009 Two-layer shallow water system: a relaxation approach. *SIAM J. Sci. Comput.* **31** (3), 1603–1627.

Anderson, T.B. & Jackson, R. 1967 Fluid mechanical description of fluidized beds. equations of motion. *Ind. Engng. Chem. Fundam.* **6** (4), 527–539.

Baker, J.L., Johnson, C.G. & Gray, J.M.N.T. 2016 Segregation-induced finger formation in granular free-surface flows. *J. Fluid Mech.* **809**, 168–212.

Bedford, A. & Drumheller, D.S. 1983 Theories of immiscible and structured mixtures. *Intl J. Engng Sci.* **21** (8), 863–960.

Berti, M., Genevois, R., LaHusen, R., Simoni, A. & Tecca, P.R. 2000 Debris flow monitoring in the acquabona watershed on the Dolomites (Italian alps). *Phys. Chem. Earth B* **25** (9), 707–715.

Bouchut, F., Fernández-Nieto, E.D., Mangeney, A. & Narbona-Reina, G. 2016 A two-phase two-layer model for fluidized granular flows with dilatancy effects. *J. Fluid Mech.* **801**, 166–221.




https://doi.org/10.1017/jfm.2025.10297 Published online by Cambridge University Press

BRUFAU, P., GARCIA-NAVARRO, P., GHILARDI, P., NATALE, L. & SAVI, F. 2000 1D mathematical modelling of debris flow. *J. Hydraul. Res.* **38** (6), 435–446.

CASTRO, M., MACÍAS, J. & PARÉS, C. 2001 A Q-scheme for a class of systems of coupled conservation laws with source term. application to a two-layer 1-D shallow water system. *ESAIM-Math. Model. Numer. Anal.* **35** (1), 107–127.

CASTRO DÍAZ, M.J., FERNÁNDEZ-NIETO, E.D., GARRES-DÍAZ, J. & DE LUNA, T.M. 2023 Discussion on different numerical treatments on the loss of hyperbolicity for the two-layer shallow water system. *Adv. Water Res.* **182**, 104587.

CHAVARRÍAS, V., SCHIELEN, R., OTTEVANGER, W. & BLOM, A. 2019 Ill posedness in modelling two-dimensional morphodynamic problems: effects of bed slope and secondary flow. *J. Fluid Mech.* **868**, 461–500.

CHAVARRÍAS, V., STECCA, G. & BLOM, A. 2018 Ill-posedness in modeling mixed sediment river morphodynamics. *Adv. Water Res.* **114**, 219–235.

CHEN, Q., SONG, D., CHEN, X., FENG, L., LI, X., ZHAO, W. & ZHANG, Y. 2024 The erosion pattern and hidden momentum in debris-flow surges revealed by simple hydraulic jump equations. *Water Resour. Res.* **60** (11), e2023WR036090.

CHIAPOLINO, A. & SAUREL, R. 2018 Models and methods for two-layer shallow water flows. *J. Comput. Phys.* **371**, 1043–1066.

CHRISTEN, M., KOWALSKI, J. & BARTELT, P. 2010 RAMMS: numerical simulation of dense snow avalanches in three-dimensional terrain. *Cold Reg. Sci. Technol.* **63** (1-2), 1–14.

CORDIER, S., LE, M.H. & MORALES DE LUNA, T. 2011 Bedload transport in shallow water models: why splitting (may) fail, how hyperbolicity (can) help. *Adv. Water Res.* **34** (8), 980–989.

DENISSEN, I.F.C., WEINHART, T., TE VOORTWIS, A., LUDING, S., GRAY, J.M.N.T. & THORNTON, A.R. 2019 Bulbous head formation in bidisperse shallow granular flow over an inclined plane. *J. Fluid Mech.* **866**, 263–297.

DOWLING, C.A. & SANTI, P.M. 2014 Debris flows and their toll on human life: a global analysis of debris-flow fatalities from 1950 to 2011. *Nat. Hazards* **71** (1), 203–227.

DREW, D.A. 1983 Mathematical modeling of two-phase flow. *Annu. Rev. Fluid Mech.* **15** (1), 261–291.

FRACCAROLLO, L. & PAPA, M. 2000 Numerical simulation of real debris-flow events. *Phys. Chem. Earth B* **25** (9), 757–763.

GEORGE, D.L. & IVERSON, R.M. 2014 A depth-averaged debris-flow model that includes the effects of evolving dilatancy II. Numerical predictions and experimental tests. *Proc. R. Soc. Lond. A Math. Phys.* **470**, 20130820.

GRAY, J.M.N.T. & KOKELAAR, B.P. 2010 Large particle segregation, transport and accumulation in granular free-surface flows. *J. Fluid Mech.* **652**, 105–137.

GRAY, J.M.N.T. & EDWARDS, A.N. 2014 A depth-averaged-rheology for shallow granular free-surface flows. *J. Fluid Mech.* **755**, 503–534.

HUTTER, K., SVENDSEN, B. & RICKENMANN, D. 1994 Debris flow modeling: a review. *Continuum Mech. Therm.* **8** (1), 1–35.

IVERSON, R.M. 1997 The physics of debris flows. *Rev. Geophys.* **35** (3), 245–296.

IVERSON, R.M. & DENLINGER, R.P. 2001 Flow of variably fluidized granular masses across three-dimensional terrain: 1. Coulomb mixture theory. *J. Geophys. Res. Solid Earth* **106** (B1), 537–552.

IVERSON, R.M. & GEORGE, D.L. 2014 A depth-averaged debris-flow model that includes the effects of evolving dilatancy I. Physical basis. *Proc. R. Soc. Lond. A Math. Phys.* **470**, 2170.

JACKSON, R. 2000 *The Dynamics of Fluidized Particles*. Cambridge University Press.

JOHNSON, C.G., KOKELAAR, B.P., IVERSON, R.M., LOGAN, M., LAHUSEN, R.G. & GRAY, J.M.N.T. 2012 Grain-size segregation and levee formation in geophysical mass flows. *J. Geophys. Res. Earth* **117** (F1), f01032.

JOP, P., FORTERRE, Y. & POULIQUEN, O. 2005 Crucial role of sidewalls in granular surface flows: consequences for the rheology. *J. Fluid Mech.* **541**, 167–192.

JOSEPH, D.D. 1990 *Fluid Dynamics of Viscoelastic Liquids*. Springer.

JOSEPH, D.D., LUNDGREN, T.S., JACKSON, R. & SAVILLE, D.A. 1990 Ensemble averaged and mixture theory equations for incompressible fluid–particle suspensions. *Intl J. Multiphase Flow* **16** (1), 35–42.

JOSEPH, D.D. & SAUT, J.C. 1990 Short-wave instabilities and ill-posed initial-value problems. *Theor. Comput. Fluid Dyn.* **1** (4), 191–227.

KOWALSKI, J. & MCELWAINE, J.N. 2013 Shallow two-component gravity-driven flows with vertical variation. *J. Fluid Mech.* **714**, 434–462.

KRVAVICA, N., TUHTAN, M. & JELENIĆ, G. 2018 Analytical implementation of Roe solver for two-layer shallow water equations with accurate treatment for loss of hyperbolicity. *Adv. Water Res.* **122**, 187–205.



https://doi.org/10.1017/jfm.2025.10297 Published online by Cambridge University Press

KURGANOV, A. & PETROVA, G. 2009 Central-upwind schemes for two-layer shallow water equations. *SIAM J. Sci. Comput.* **31** (3), 1742–1773.

KURGANOV, A. & TADMOR, E. 2000 New high-resolution central schemes for nonlinear conservation laws and convection–diffusion equations. *J. Comput. Phys.* **160** (1), 241–282.

LANGHAM, J., WOODHOUSE, M.J., HOGG, A.J. & PHILLIPS, J.C. 2021 Linear stability of shallow morphodynamic flows. *J. Fluid Mech.* **916**, A31.

LI, J., CAO, Z., HU, K., PENDER, G. & LIU, Q. 2018 A depth-averaged two-phase model for debris flows over fixed beds. *Intl. J. Sediment Res.* **33** (4), 462–477.

MACEDONIO, G. & PARESCHI, M.T. 1992 Numerical simulation of some lahars from Mount St. Helens. *J. Volcanol. Geotherm. Res.* **54** (1–2), 65–80.

MAXEY, M.R. & RILEY, J.J. 1983 Equation of motion for a small rigid sphere in a nonuniform flow. *Phys. Fluids* **26** (4), 883–889.

MCCOY, S.W., KEAN, J.W., COE, J.A., STALEY, D.M., WASKLEWICZ, T.A. & TUCKER, G.E. 2010 Evolution of a natural debris flow: in situ measurements of flow dynamics, video imagery, and terrestrial laser scanning. *Geology* **38** (8), 735–738.

MENG, X., JOHNSON, C.G. & GRAY, J.M.N.T. 2022 Formation of dry granular fronts and watery tails in debris flows. *J. Fluid Mech.* **943**, A19.

MENG, X., TAYLOR-NOONAN, A.M., JOHNSON, C.G., TAKE, W.A., BOWMAN, E.T. & GRAY, J.M.N.T. 2024 Granular-fluid avalanches: the role of vertical structure and velocity shear. *J. Fluid Mech.* **980**, A11.

MEYRAT, G., MCARDELL, B., IVANOVA, K., MÜLLER, C. & BARTELT, P. 2022 A dilatant, two-layer debris flow model validated by flow density measurements at the Swiss illgraben test site. *Landslides* **19** (2), 265–276.

MORLAND, L.W. 1992 Flow of viscous fluids through a porous deformable matrix. *Surv. Geophys.* **13** (3), 209–268.

OVSYANNIKOV, L.V. 1979 Two-layer "shallow water" model. *J. Appl. Mech. Tech. Phys.* **20** (2), 127–135.

PAILHA, M. & POULIQUEN, O. 2009 A two-phase flow description of the initiation of underwater granular avalanches. *J. Fluid Mech.* **633**, 115–135.

PELANTI, M., BOUCHUT, F. & MANGENEY, A. 2008 A Roe-type scheme for two-phase shallow granular flows over variable topography. *ESAIM-Math. Model. Numer. Anal.* **42** (5), 851–885.

PIERSON, T.C. 1995 Flow characteristics of large eruption-triggered debris flows at snow-clad volcanoes: constraints for debris-flow models. *J. Volcanol. Geotherm. Res.* **66** (1), 283–294.

PITMAN, E.B. & LE, L. 2005 A two-fluid model for avalanche and debris flows. *Phil. Trans. R. Soc. Lond. A* **363** (1832), 1573–1601.

POULIQUEN, O. & FORTERRE, Y. 2002 Friction law for dense granular flows: application to the motion of a mass down a rough inclined plane. *J. Fluid Mech.* **453**, 133–151.

PUDASAINI, S.P. 2012 A general two-phase debris flow model. *J. Geophys. Res. Earth* **117** (F3), F03010.

PUDASAINI, S.P. & MERGILI, M. 2019 A multi-phase mass flow model. *J. Geophys. Res. Earth* **124** (12), 2920–2942.

SARNO, L., CARRAVETTA, A., MARTINO, R., PAPA, M.N. & TAI, Y.-C. 2017 Some considerations on numerical schemes for treating hyperbolicity issues in two-layer models. *Adv. Water Res.* **100**, 183–198.

SAVAGE, S.B. & HUTTER, K. 1989 The motion of a finite mass of granular material down a rough incline. *J. Fluid Mech.* **199**, 177–215.

SCHÖFFL, T., NAGL, G., KOSCHUCH, R., SCHREIBER, H., HÜBL, J. & KAITNA, R. 2023 A perspective of surge dynamics in natural debris flows through pulse-doppler radar observations. *J. Geophys. Res. Earth* **128** (9), e2023JF007171.

SHIEH, C.-L., JAN, C.-D. & TSAI, Y.-F. 1996 A numerical simulation of debris flow and its application. *Nat. Hazards* **13** (1), 39–54.

STECCA, G., SIVIGLIA, A. & BLOM, A. 2014 Mathematical analysis of the Saint– Venant–Hirano model for mixed-sediment morphodynamics. *Water Resour. Res.* **50** (10), 7563–7589.

TAKAHASHI, T., NAKAGAWA, H., HARADA, T. & YAMASHIKI, Y. 1992 Routing debris flows with particle segregation. *J. Hydraul. Engng* **118** (11), 1490–1507.

TROWBRIDGE, J.H. 1987 Instability of concentrated free surface flows. *J. Geophys. Res. Oceans* **92** (C9), 9523–9530.

TRUJILLO-VELA, M.G., RAMOS-CAÑÓN, A.M., ESCOBAR-VARGAS, J.A. & GALINDO-TORRES, S.A. 2022 An overview of debris-flow mathematical modelling. *Earth Sci. Rev.* **232**, 104135.

VREUGDENHIL, C.B. 1979 Two-layer shallow-water flow in two dimensions, a numerical study. *J. Comput. Phys.* **33** (2), 169–184.



https://doi.org/10.1017/jfm.2025.10297 Published online by Cambridge University Press

WOODHOUSE, M.J., THORNTON, A.R., JOHNSON, C.G., KOKELAAR, B.P. & GRAY, J.M.N.T. 2012 Segregation-induced fingering instabilities in granular free-surface flows. *J. Fluid Mech.* **709**, 543–580.

ZANUTTIGH, B. & LAMBERTI, A. 2007 Instability and surge development in debris flows. *Rev. Geophys.* **45** (3), RG3006.

https://doi.org/10.1017/jfm.2025.10297 Published online by Cambridge University Press